# Spatial and Temporal Patterns in Petrogenic Organic Carbon Mobilisation during the Paleocene-Eocene Thermal Maximum

**E. H. Hollingsworth[1*], F. J. Elling[2,3], M. P. S. Badger[4], R. D. Pancost[5], A. J. Dickson[4,6], R. L. Rees-Owen[5], N. M. Papadomanolaki[7,8], A. Pearson[2], A. Sluijs[7], K. H. Freeman[9], A. A. Baczynski[9], G. L. Foster[1], J. H. Whiteside[1,10], and G. N. Inglis[1*]**

[1] School of Ocean and Earth Science, University of Southampton, Southampton, UK

[2] Department of Earth and Planetary Sciences, Harvard University, Cambridge, MA, USA

[3] Leibniz-Laboratory for Radiometric Dating and Isotope Research, Christian-Albrechts, University of Kiel, Kiel, Germany

[4] School of Environment, Earth and Ecosystem Sciences, The Open University, Milton Keynes, UK

[5] Department of Earth Sciences and School of Chemistry, University of Bristol, Bristol, UK

[6] Centre of Climate, Ocean and Atmosphere, Department of Earth Sciences, Royal Holloway University of London, Surrey, UK

[7] Department of Earth Sciences, Utrecht University, Utrecht, Netherlands

[8] Now at Institue für Geologie and Paläontologie, Universität Münster, Münster, Germany

[9] Department of Geosciences, The Pennsylvania State University, State College, PA, USA

[10] Now at Department of Earth and Environmental Sciences, San Diego State University, San Diego, CA, USA

*Corresponding author: Gordon N. Inglis (Gordon.inglis@soton.ac.uk) and Emily H. Hollingsworth (e.hollingsworth@soton.ac.uk)

**Key Points:**

1. We assess spatial and temporal patterns in petrogenic organic carbon ($OC_{petro}$) mobilisation during the Paleocene-Eocene Thermal Maximum
2. Evidence for enhanced $OC_{petro}$ mobilisation in the subtropics and mid-latitudes, likely due to an increase in extreme rainfall events
3. $OC_{petro}$ mobilisation remained elevated during the recovery phase of the Paleocene-Eocene Thermal Maximum

## Abstract

The Paleocene-Eocene Thermal Maximum (PETM) was a transient global warming event and is recognised in the geologic record by a prolonged negative carbon isotope excursion (CIE). The onset of the CIE was due to a rapid influx of $^{13}C$-depleted carbon into the ocean-atmosphere system. However, the mechanisms required to sustain the negative CIE remains unclear. Enhanced mobilisation and oxidation of petrogenic organic carbon ($OC_{petro}$) has been invoked to explain elevated atmospheric carbon dioxide concentrations after the onset of the CIE. However, existing evidence is limited to the mid-latitudes and subtropics. Here, we determine whether: (i) enhanced mobilisation and subsequent burial of $OC_{petro}$ in marine sediments was a global phenomenon; and (ii) whether it occurred throughout the PETM. To achieve this, we utilise a lipid biomarker approach to trace and quantify $OC_{petro}$ burial in a global compilation of PETM-aged shallow marine sites ($n$ = 7, including five new sites). Our results confirm that $OC_{petro}$ mass accumulation rates (MARs) increased within the subtropics and mid-latitudes during the PETM, consistent with evidence of higher physical erosion rates and intense episodic rainfall events. High-latitude sites do not exhibit drastic changes in the source of organic carbon during the PETM and $OC_{petro}$ MARs increase slightly or remain stable, perhaps due a more stable hydrological regime. Crucially, we also demonstrate that $OC_{petro}$ MARs remained elevated during the recovery phase of the PETM. Although $OC_{petro}$ oxidation was likely an important positive feedback mechanism throughout the PETM, we show that this feedback was both spatially and temporally variable.



## Plain Language Summary

The Paleocene-Eocene Thermal Maximum (PETM) was the most severe global warming event of the last 66 million years and was caused by the rapid release of greenhouse gases into the atmosphere. However, scientists have been unable to determine why the PETM lasted for > 100,000 years. Here, we test whether $CO_2$ released from the erosion, transport, and oxidation of ancient rock-derived (or petrogenic) organic carbon can explain the long duration of the PETM. We also aim to identify if this occurred globally and/or throughout the PETM. We achieve this by looking at biomarkers (molecular fossils) and use this approach to ‘fingerprint’ the input of petrogenic organic carbon into the marine realm. Our results suggest enhanced transport of

petrogenic organic carbon was restricted to the subtropics and mid-latitudes, with limited changes in the high-latitudes. We also find evidence for erosion and transport of petrogenic organic carbon throughout the PETM. Therefore, this process likely contributed to increasing atmospheric $CO_2$ levels and may have been an important positive feedback mechanism in past and future warm climates.

## 1 Introduction

Climate and tectonics have modulated the flux of carbon to and from terrestrial reservoirs over geological timescales. Early studies predominantly focused on understanding the role of inorganic carbon, for example, carbon dioxide ($CO_2$) released from solid Earth degassing versus $CO_2$ drawdown from silicate weathering (e.g., Berner et al., 1983; Caldeira & Berner, 1997; Walker et al., 1981). However, the past two decades have highlighted the importance of the terrestrial organic carbon cycle as a climate feedback mechanism (Hilton & West, 2020). Whether it acts as a positive or negative feedback mechanism largely depends on whether the organic carbon (OC) is 'biospheric' ($OC_{bio}$), representing relatively recent thermally immature organic carbon ($10^2$–$10^4$ years old; e.g., vegetation and soils), or 'petrogenic' ($OC_{petro}$), representing ancient rock-derived and thermally mature organic carbon (> $10^6$ years old; e.g., organic carbon-rich shales). Erosion, mobilisation, and the subsequent burial of $OC_{bio}$ in marine sediments helps to sequester $CO_2$ (Berhe et al., 2007; Stallard, 1998). In contrast, exhumation and oxidation of $OC_{petro}$ during lateral transport from land-to-sea can release $CO_2$ (Petsch et al., 2000). In modern settings, up to ~90 % of $OC_{petro}$ is oxidised in large catchments, such as the Amazon and Himalayan range (e.g., Bouchez et al., 2010; Galy et al., 2008), whereas a lower proportion (~10–40 %) of $OC_{petro}$ is oxidised in mountain basins with steep rivers (e.g., Hilton et al., 2011, 2014). Crucially, regardless of individual catchment dynamics, $OC_{petro}$ has the potential to be oxidised and increase atmospheric $CO_2$ concentrations.

Several studies have quantified the mobilisation and burial of $OC_{petro}$ in modern systems (e.g., Blair et al., 2003; Clark et al., 2017, 2022; T. I. Eglinton et al., 2021 and references therein; Galy et al., 2007, 2015 and references therein; Hilton et al., 2010, 2011; Hilton & West, 2020 and references therein; Smith et al., 2013) and Holocene sediments (e.g., Hilton et al., 2015; Kao et al., 2008, 2014). These studies show that erosion and transport of $OC_{petro}$ is largely controlled by

a combination of geomorphic and climate processes (e.g., T. I. Eglinton et al., 2021; Hilton, 2017). For example, extreme rainfall events can trigger bedrock landslides (e.g., Hilton et al., 2008) and/or create deeply incised gullies (e.g., Leithold et al., 2006), both of which can expose $OC_{petro}$ to oxidation. However, clastic sediments from hyperpycnal flows and turbidites can act to enhance the preservation of $OC_{petro}$ (e.g., Bouchez et al., 2014; Hilton et al., 2011). As climate model simulations indicate an intensification of the hydrological cycle in response to rising atmospheric $CO_2$ levels and global temperatures (Lee et al., 2021), the delivery of $OC_{petro}$ to the oceans will likely be enhanced in the future. However, such predictions are based on present-day observations and/or past climate states that span a lower-than-modern atmospheric $CO_2$ values (e.g., Hilton & West, 2020; Kao et al., 2008).

The geological record enables investigations into high $CO_2$ states of the past, providing unique insights into how terrestrial carbon cycle processes may operate in the future. Many studies have focused on the Paleocene-Eocene Thermal Maximum (PETM; ~56 million years ago) (McInerney & Wing, 2011), a transient carbon cycle perturbation characterised by global warming (~4–6 ºC; Inglis et al., 2020; Tierney et al., 2022) and an intensified hydrological cycle (Carmichael et al., 2017 and references therein). The PETM is identified in the geologic record by a negative carbon isotope excursion (CIE) (e.g., -4 ± 0.4 ‰; Elling et al., 2019). The onset of the PETM is on the order-of-millennia (Kirtland Turner, 2018; Zeebe et al., 2014) and is followed by sustained low and stable carbon isotope ($\delta^{13}C$) values for ~94–170 thousand years (kyrs) (Zeebe & Lourens, 2019), referred to as the "body" of the CIE (Bowen et al., 2006). The body is then followed by a long recovery of ~50–120 kyrs (Bowen, 2013; Murphy et al., 2010; Zeebe et al., 2009), which is further divided into Phase I (initial rapid rise in $\delta^{13}C$) and Phase II (final gradual rise in $\delta^{13}C$) (Röhl et al., 2007).

The onset of the CIE was the result of a rapid influx of $^{13}C$-depleted carbon from one or more reservoirs outside the active global exogenic carbon pool (Dickens et al., 1997). Proposed reservoirs include submarine methane hydrates (Dickens, 2011; Dickens et al., 1995), terrestrial organic carbon (Bowen, 2013; Deconto et al., 2012; Kurtz et al., 2003), and volcanic carbon related to the North Atlantic Igneous Province (Gutjahr et al., 2017; Jones et al., 2019; Storey et

al., 2007; Svensen et al., 2004). Less explored are the mechanisms responsible for the prolonged body of the CIE. This feature requires continual input of $^{13}C$-depleted carbon (e.g., Zeebe et al., 2009), thus several feedback mechanisms (either acting individually or in combination) have been proposed. This includes a slow dissociation of oceanic methane hydrates (Zeebe, 2013), pulsed releases of thermogenic methane from vent complexes (e.g., Frieling et al., 2016; Kirtland Turner, 2018), and/or 'leaky' terrestrial organic carbon reservoirs (Bowen, 2013). Alternatively, recent work suggests that $CO_2$ released from $OC_{petro}$ oxidation could explain the extended body of the CIE (Lyons et al., 2019). This theory is based on evidence for an order-of-magnitude increase in the delivery of $OC_{petro}$ to the oceans, ~10–20 kyrs after the onset of the PETM. However, this study was limited to the mid-latitudes (Atlantic Coastal Plain) and subtropics (Tanzania), and therefore may not be globally representative. It is also unclear whether enhanced mobilisation of $OC_{petro}$ was a persistent feature throughout the PETM or whether it was restricted to the body interval.

Here, we use lipid biomarker thermal maturity ratios to fingerprint $OC_{petro}$ burial in a global compilation of PETM-aged shallow marine sites (n = 7, including five new sites). Lipid biomarkers undergo various structural alterations with increasing thermal maturity (e.g., defunctionalisation, isomerisation, catagenesis, and aromatisation; Peters et al., 2005) and thus can be used to assess the proportion of $OC_{petro}$ in marine sediments (Lyons et al., 2019). We focus on thermally immature, shallow marine sediments as they are 'hotspots' for terrestrial organic carbon input (Bianchi et al., 2018). We quantify $OC_{petro}$ burial fluxes before and during the PETM, using a two endmember mixing model. Overall, we aim to determine whether: (i) enhanced mobilisation and subsequent burial of $OC_{petro}$ in the ocean was a global phenomenon; and (ii) whether it occurred throughout the PETM.

## 2 Methods

### 2.1 Data compilation

New *n*-alkane- and/or hopane-based thermal maturity ratios were acquired from the following PETM-aged shallow marine sites: the International Ocean Drilling Program Expedition 302 Site M0004A (or the Arctic Coring Expedition; **ACEX**); the Ocean Drilling Program Site 1172 Hole D (**ODP Site 1172**); **Kheu River**; ODP Leg 174AX Ancora Site Hole A/B (**Ancora**); and the

Tanzania Drilling Project Site 14 Hole A (**TDP Site 14**) (Figure 1). Additional information (e.g., paleodepth) and a brief description of the lithology for each site can be found within Table S1 and Text S1 of the supporting information, respectively. We also compile *n*-alkane- and/or hopane-based thermal maturity ratios from the following published PETM-aged shallow marine sites: TDP Site 14 (Carmichael et al., 2017; Handley et al., 2012); South Dover Bridge (**SDB**) (Lyons et al., 2019); and Cambridge-Dorchester Airport (**CamDor**) (Lyons et al., 2019) (Figure 1). Other published biomarker records are available for PETM-aged shallow marine sites, however these sequences are dominated by autochthonous $OC_{petro}$ and show evidence for post-depositional diagenesis (Cui et al., 2021; Handley et al., 2011).

### 2.2 Organic geochemistry

For this study, samples from ACEX (n = 94), ODP Site 1172 (n = 41), and Ancora (n = 42) were freeze dried, homogenized, and extracted using a MARS5 microwave-assisted extraction system, with: (i) dichloromethane:methanol (DCM:MeOH; 1:1, *v*:*v*); (ii) DCM:MeOH (9:1, *v*:*v*); and (iii) DCM, at Harvard University (see Elling et al., 2019). Each solvent mixture was heated for 30 minutes to 100 °C, followed by a hold time of 20 minutes. The extracts from the three steps were combined into a total lipid extract (TLE) and further divided into five fractions (following Polik et al., 2018). At the University of Southampton, extracted copper was added to the apolar fractions for 24 hours to remove elemental sulphur. The apolar fractions were then analysed using a ThermoFisher Trace 1310 GC coupled to a Thermo TSQ8000 Triple Quadrupole MS (GC-MS). Helium was used as the carrier gas and separation was achieved with DB-5 column (30 m x 0.25 mm i.d., 0.25 μm film thickness). The GC oven program started at 70 °C for 1 minute, increased to 130 °C at 20 °C $min^{-1}$, followed by 300 °C at 4 °C $min^{-1}$, which was then held for 20 minutes. MS scanning occurred between mass-to-charge ratio (*m/z*) 50 to 650 Daltons, and an ionisation energy of 70 eV. Compound identification was based on retention times, fragmentation patterns, comparison to an in-house standard, and library matches.

Kheu River samples (n = 39) were extracted at the University of Bristol by ultrasonicating homogenised samples sequentially with DCM, DCM:MeOH (1:1, *v*:*v*), and MeOH. Elemental sulphur was removed from the combined TLE using activated copper turnings. An activated silica column with saturated ammonia in chloroform and chloroform:acetic acid (100:1, *v*:*v*) was

used to separate the neutral and acid fraction, respectively. The apolar fraction was split from the neutral fraction by eluting with hexane:DCM (9:1, *v*:*v*) via separation on an alumina column. The apolar fractions were then analysed at the University of Bristol on a Thermoquest Finnigan Trace GC interfaced with a Thermoquest Finnigan Trace MS. The GC was fitted with a fused capillary column (50 m x 0.32 mm i.d.) and the carrier gas was helium. The samples were suspended in ethyl acetate and injected at 70 °C. The temperature program increased to 130 °C (20 °C $min^{-1}$), then 300 °C (4 °C $min^{-1}$), and finally remained isothermal for 20 minutes. The MS operated with an electron ionisation source at 70 eV, scanning over *m/z* ranges of 50 to 850 Daltons. The compounds were integrated on the total ion chromatogram (TIC).

Additional samples (n = 12) from TDP Site 14 were homogenised and extracted at the University of Bristol. Extractions were achieved via Soxhlet apparatus overnight, using DCM:MeOH (2:1 *v:v*). The apolar fraction was suspended in hexane:DCM (9:1, *v:v*) and separated by alumina column chromatography. Co-eluting compounds and/or unresolved complex mixtures were reduced with urea adduction (following Pancost et al., 2008). Elemental sulphur was removed using extracted copper turnings. The apolar fractions were analysed at the University of Bristol on the same GC-MS as used for Kheu River. The GC was fitted with a CPsil-5CB column (Agilent Technologies, dimethylpolysiloxane stationary phase) and the carrier gas was helium. The samples were injected in ethyl acetate at 70 °C. The temperature program increased to 130 °C (20 °C $min^{-1}$), then 300 °C (4 °C $min^{-1}$), and finally held for 25 minutes. The MS operated with an electron ionisation source at 70 eV, scanning over *m/z* ranges of 50 to 850 Daltons. The compounds were integrated on the TIC or using the appropriate mass fragment (e.g., *m/z* 191).

### 2.3 Lipid biomarker proxies

#### 2.3.1 *n*-alkane-based thermal maturity ratios

Modern plants and sediments contain long-chain *n*-alkanes with an odd-over-even preference (G. Eglinton & Hamilton, 1967), however this is progressively lost during diagenesis. The shift away from a dominance of long-chain *n*-alkanes with an odd-over-even predominance is captured by the carbon preference index (CPI) (Bush & McInerney, 2013). Modern sediments exhibit high CPI values (> 3–30), indicating relatively unaltered thermally immature organic matter

(Diefendorf & Freimuth, 2017). In contrast, mature organic matter (e.g., coal, oil) exhibits low CPI values (~1). CPI values < 1 are less common, and typify low-maturity source rocks from carbonates or hypersaline environments. In this study, sites with extensive post-depositional diagenesis were excluded, such that CPI values closer to 1 likely suggests input of allochthonous thermally mature organic matter (e.g., $OC_{petro}$). Here, we use the equation as originally defined by Bray & Evans (1961):

$$\mathrm{CPI} = \frac{1}{2}\left[\left(\frac{\sum_{\mathrm{odd}}(C_{25-31})}{\sum_{\mathrm{even}}(C_{26-32})}\right) + \left(\frac{\sum_{\mathrm{odd}}(C_{27-33})}{\sum_{\mathrm{even}}(C_{26-32})}\right)\right] \qquad \text{(Eq. 1)}$$

### 2.3.2 Hopane-based thermal maturity ratios

Hopanes are the diagenetic products of biohopanoids, which are produced by a wide diversity of bacteria and consequently ubiquitous in a range of environments (Kusch & Rush, 2022). The ratios between different hopanes and their various stereoisomers have long been utilised as a thermal maturity proxy in the field of petroleum geochemistry (e.g., Farrimond et al., 1998; Mackenzie et al., 1980). Most of the hopane-based thermal maturity ratios used in this study are normalised (with the exception of Equation 4). Values indicating high thermal maturity likely suggests allochthonous older material (e.g., pre-PETM-aged $OC_{petro}$), as sites with post-depositional diagenesis were excluded from this study. We use a multi-ratio approach as each ratio corresponds to different stages of maturity relative to the oil window (i.e., from early diagenesis to the generation of oil), thus enabling insight on the degree of thermal maturation (Figure S1 in the supporting information). However, hopane distributions also vary depending on the lithofacies and/or depositional environment (Peters et al., 2005). Therefore, without knowledge of the source rock at each locality, comparison between the sites should be undertaken with caution.

With the exception of *Frankia* spp. (Rosa-Putra et al., 2001), all bacteria synthesise hopanoids with a 17β,21β configuration. However, this changes to a more stable βα and then αβ configuration during early diagenesis and then peak oil generation, respectively (Farrimond et al., 1998; Mackenzie et al., 1980). The shift from ββ to αβ is expressed via the following equation (sometimes referred in literature as ‘hopanoid isomerisation’):

$\alpha\beta/(\alpha\beta + \beta\beta)$ (Eq. 2)

Higher thermal maturity is marked by values closer to 1. This equation is applied to the hopanes that contained both isomers (i.e., mostly $C_{29\text{-}31}$ hopanes). However, caution should be taken when interpreting sediments with input from peats, as $C_{31}$ αβ isomers dominate the hopane distribution within acidic wetland environments (Inglis et al., 2018).

The shift from βα (also referred to as moretane; M) to the more stable αβ (also referred to as hopane; H) is assessed via the following equation (sometimes referred in literature as 'moretane/hopane ratio'):

$\beta\alpha/(\beta\alpha + \alpha\beta)$ (Eq. 3)

This equation is applied to the most commonly used $C_{30}$ hopane (e.g., French et al., 2012), as well as the less commonly used $C_{29}$ hopane (Peters et al., 2005). Values closer to ~0 indicate higher thermal maturity and oil generation.

The $C_{29}$ αβ hopane (also referred to as norhopane; N) is more thermally stable than $C_{30}$ αβ hopane. This is assessed via the following equation (sometimes referred in literature as 'norhopane/hopane ratio'):

$C_{29}\ \alpha\beta/C_{30}\ \alpha\beta$ (Eq. 4)

As well as a thermal maturity proxy, this ratio has been utilised to differentiate between anoxic carbonate and/or marl source rocks (> 1) vs. clay-rich source rocks (< 1) (Peters et al., 2005).

Towards the early stages of oil generation, there is a change in stereochemistry at the C-22 position, from the biologically favoured R configuration to a near equal mix of R and S (Farrimond et al., 1998; Mackenzie et al., 1980; Peters et al., 2005). This is expressed via the following equation (sometimes referred in literature as 'homohopane isomerisation'):

$S/(S + R)$ (Eq. 5)

This equation uses $C_{31\text{-}35}$ hopanes (also referred to as homohopanes) and approaches maximum (equilibrium) values of ~0.6 as thermal maturity increases and oil is generated.

At the late stage of oil generation, $C_{27}$ hopanes shift in the position of a D-ring methyl group, from C-18 (17α(H),22,29,30-trisnorhopane; $T_m$) to C-17 (18α(H),22,29,30-trisnorneohopane; $T_s$) (Farrimond et al., 1998; Peters et al., 2005). This is expressed via the following equation:

$$T_s/(T_s + T_m) \qquad \text{(Eq. 6)}$$

$T_m$ refers to maturable (less stable), whereas $T_s$ denotes stable. Values closer to 1 indicate higher thermal maturity, although the oxicity of the depositional environment also has a notable influence (Peters et al., 2005).

### 2.4 Two-endmember mixing models

The fraction of $OC_{petro}$ ($f_{petro}$) was calculated for each hopane-based thermal maturity ratio ($X_{mix}$; Table 1), following the two endmember mixing model from Lyons et al. (2019):

$$X_{\text{mix}} = f_{\text{petro}} \times X_{\text{petro}} + \left(1 - f_{\text{petro}}\right) \times X_{\text{background}} \qquad \text{(Eq. 7)}$$

where $X_{background}$ and $X_{petro}$ is the defined immature and mature endmembers, respectively. The endmembers for $C_{31\text{-}35}$ S/(S+R) ratio follow the definitions in Lyons et al. (2019), where $X_{background}$ is the contemporaneous carbon value of 0 and $X_{petro}$ is the most thermally mature value of 0.6. The endmembers for $C_{29\text{-}30}$ βα/(βα + αβ) ratio also follow the definitions in Lyons et al. (2019), where $X_{background}$ is 1 and $X_{petro}$ is 0. For this study, the endmembers of the αβ/(αβ + ββ) ratio was defined as 0 for $X_{background}$ and 1 for $X_{petro}$. Note that $C_{29}$ αβ/$C_{30}$ αβ and $T_s/(T_s + T_m)$ ratios were excluded due to their strong dependence on the source rock and/or depositional environment (Peters et al., 2005).

Table 1: The hopane-based thermal maturity ratio ($X_{mix}$) used to calculate $f_{petro}$, with assumed linear sedimentation rate (LSR) and organic carbon content (%) (reported either as total organic carbon (TOC) or $C_{org}$) reference for each site

| Site | $X_{mix}$ | LSR (cm kyr$^{-1}$) | | | | Organic carbon content (%) References |
|---|---|---|---|---|---|---|
| | | Pre-PETM | Core PETM | Recovery PETM | | |
| | | | | Phase I | Phase II | |
| ACEX[a] | $C_{30\text{-}31}$ αβ/(αβ + ββ)<br>$C_{31}$ S/(S + R)<br>$C_{30}$ βα/(βα + αβ) | 1 | Min: 3.8<br>Max: 6.2 | | | TOC<br>Elling et al. (2019) |
| ODP Site 1172[b] | $C_{30\text{-}31}$ αβ/(αβ + ββ)<br>$C_{31}$ S/(S + R)<br>$C_{30}$ βα/(βα + αβ) | 0.57 | Min: 0.4<br>Max: 0.5 | Not available | | $C_{org}$<br>Papadomanolaki et al. (2022) |
| Kheu River[c] | $C_{29\text{-}31}$ αβ/(αβ + ββ)<br>$C_{29\text{-}30}$ βα/(βα + αβ) | 0.3 | 1.9 | | | $C_{org}$<br>Dickson et al. (2014) |
| Ancora[d] | $C_{30\text{-}31}$ αβ/(αβ + ββ)<br>$C_{31}$ S/(S + R)<br>$C_{30}$ βα/(βα + αβ) | 0.8 | 11.2 and 4.3 | 1.3 | 8.4 | TOC<br>Elling et al. (2019) |
| TDP Site 14[e] | $C_{29\text{-}31}$ αβ/(αβ + ββ)<br>$C_{31\text{-}35}$ S/(S + R)<br>$C_{29\text{-}30}$ βα/(βα + αβ) | Min: 0.5<br>Max: 2 | Min: 3.5<br>Max: 14 | NA | | $C_{org}$<br>Aze et al. (2014) |
| SDB[f] | $C_{31}$ S/(S + R)<br>$C_{29}$ βα/(βα + αβ)* | Min: 1.03<br>Max: 2.4 | 14 | 21.3 | 21.3 | TOC<br>Lyons et al. (2019) |
| CamDor[f] | $C_{29}$ βα/(βα + αβ)*<br>$C_{31\text{-}32}$ S/(S + R)* | Min: 1.03<br>Max: 2.4 | 14 | | | TOC<br>Lyons et al. (2019) |

[a-f]References for LSR. [a]Sluijs, Röhl, et al. (2008). [b]Sluijs et al. (2011). [c]John et al. (2008). [d]Stassen et al. (2012). [e]Lyons et al. (2019). [f]Doubrawa et al. (2022).

*$f_{petro}$ calculated in Lyons et al. (2019)

### 2.5 Mass accumulation rates

The mass accumulation rate (MAR; in gC cm$^2$ kyr$^{-1}$) of $OC_{petro}$ was calculated for all the new and published $f_{petro}$ data, following Lyons et al. (2019):

$$MAR = LSR \times \rho \times f_{petro} \times \frac{TOC}{100} \qquad \text{(Eq. 8)}$$

, where LSR is the linear sedimentation rate (cm kyr$^{-1}$), $\rho$ is the dry bulk density (g cm$^{-3}$), and TOC is the total organic carbon (TOC) or $C_{org}$ (%) (see Table 1). As published bulk density

values are only available for one site (ODP Site 1172), a constant $\rho$ value of 1.8g $cm^{-3}$ was assumed across all the sites (following Dunkley-Jones et al., 2017). However, we acknowledge that changes in dry bulk density may influence absolute MARs, especially in sites with major lithological changes (see Text S1). The TOC values and LSR were acquired for each location from previously published studies (Table 1). $C_{org}$ records from ODP Site 1172 (Papadomanolaki et al., 2022) and TDP Site 14 (Aze et al., 2014) were linearly interpolated to match the depths of the biomarker data, using R Package Astrochron (Meyers, 2014). LSR estimates were obtained (where possible) for three key time intervals: (i) pre-PETM (Paleocene); (ii) the "core" (onset and body of the CIE) of the PETM; (iii) and the recovery of the PETM (see Text S1 in the supporting information). This was available for all the sites with the exception of ODP Site 1172, which lacks the recovery interval. Note that the recovery at Ancora and SDB were further divided into: (iiia) Phase I; and (iiib) Phase II. Kheu River does not have LSR data, thus estimates were taken from the nearby Aktumsuk section (Uzbekistan; John et al., 2008). Both Kheu River and Aktumsuk comprises shallow marine deposits that exhibits TOC values from ~0.1 % pre-PETM to a maximum of ~8.5 % during the PETM (Bolle et al., 2000; Dickson et al., 2014). Similarly, LSRs from within the core interval of SDB was assumed to be the same for the entire PETM section at CamDor (following Lyons et al., 2019).

## 3 Results

### 3.1 Thermal maturity ratios

#### 3.1.1 ACEX

The apolar fraction contains short- ($C_{15\text{-}19}$), mid- ($C_{21\text{-}25}$), and long- ($C_{27\text{-}33}$) chain *n*-alkanes, and $C_{27}$ to $C_{32}$ hopanes (including αβ, βα, and ββ isomers). Both the CPI (ranging from ~1–3; Figure 2b) and hopane-based thermal maturity ratios exhibit relatively stable trends throughout the sequence, suggesting that the organic carbon source did not distinctly change. Note that potential information may be missing due poor core recovery between ~388–384.5 mcd (Sluijs et al., 2006). However, $C_{30}$ αβ/(αβ + ββ) (Figure 2c), $C_{31}$ S/(S + R) (Figure 2d), and $T_s/(T_s + T_m)$ (Figure 2f) values slightly increase (i.e., higher thermal maturity) between pre-PETM and the core of the PETM, by an average of 0.01, 0.01, and 0.08, respectively. These indices then decline during the recovery interval. $C_{31}$ αβ/(αβ + ββ) and $C_{30}$ βα/(βα + αβ) ratios (Figure 2c) exhibit the

opposite trend, with lower thermal maturity during the core interval and the $C_{30}$ βα/(βα + αβ) ratio (Figure 2e) continuing to decline into the recovery of the PETM.

### 3.1.2 ODP Site 1172

The apolar fraction contains $C_{16}$ to $C_{34}$ *n*-alkanes and the CPI has a mean value of 2.8. Samples with CPI > 3 (i.e., relatively low thermal maturity), are mostly constrained to the pre-PETM interval (Figure 3b). Hopanes range from $C_{27}$ to $C_{32}$ (including αβ, βα, and ββ isomers), and the thermal maturity ratios exhibit a relatively stable trend throughout the sequence. However, the $C_{31}$ S/(S + R) ratio slightly increases by 0.09 during the core interval and into the recovery of the PETM (Figure 3d), suggesting potential input of thermally mature organic carbon. $C_{30}$ αβ/(αβ + ββ) (Figure 3c), $C_{31}$ αβ/(αβ + ββ) (Figure 3c), and $C_{30}$ βα/(βα + αβ) (Figure 3e) values exhibit the opposite behaviour, shifting towards relatively hermally immature values during the core of the PETM, by an average of 0.19, 0.22, and 0.07, respectively. During the recovery, $C_{30}$ αβ/(αβ + ββ) (Figure 3c), $C_{31}$ αβ/(αβ + ββ) (Figure 3c), and $C_{30}$ βα/(βα + αβ) (Figure 3e) ratios return to relatively more thermally mature values.

### 3.1.3 Kheu River

$C_{16}$ to $C_{35}$ *n*-alkanes were identified in the apolar fraction, in addition to $C_{27}$ to $C_{31}$ hopanes (including αβ, βα, and ββ isomers). Prior to the PETM and during the recovery, the CPI drops below 1 (Figure 4b), which may suggest input of low-maturity source rocks from carbonates or hypersaline environments. The CPI also oscillate drastically between ~1 and ~3 within the lower depths of the core of the PETM (~0–50 cm; Figure 4b). This section of high variability is also reflected in the $C_{29}$ αβ/$C_{30}$ αβ (Figure 4d) and $C_{29}$ βα/(βα + αβ) (Figure 4e) ratios, suggesting rapid changes in the organic carbon source. However, it may also represent greater sampling resolution within the PETM. Overall, the average of all the thermal maturity ratios exhibit lower thermal maturity during the core interval. In addition, the $C_{29}$ αβ/$C_{30}$ αβ ratio present values > 1 during the PETM (Figure 4d), potentially indicating input from a clay-rich source rock. With the exception of $T_s/(T_s + T_m)$ (Figure 4f), all of the ratios increase in higher thermal maturity during the recovery to either higher than pre-PETM (i.e., $C_{29}$ αβ/($C_{29}$ αβ + $C_{30}$ αβ) and $C_{29\text{-}30}$ βα/(βα + αβ) ratios) or near pre-PETM values (i.e., $C_{29\text{-}31}$ αβ/(αβ + ββ) ratio).

373 3.1.4 Ancora

374 The apolar fraction contains $C_{15}$ to $C_{34}$ *n*-alkanes and $C_{27}$ to $C_{31}$ hopanes (including αβ, βα, and
375 ββ isomers). CPI ranges from 1–2.2 and is similar during the pre-PETM and PETM interval
376 (Figure 5b). Similarly, $C_{30\text{-}31}$ αβ/(αβ + ββ) values remain relatively constant, albeit exhibiting a
377 very slight decline by an average of 0.01–0.03 (i.e., decreasing thermal maturity; Figure 5c). On
378 the other hand, $C_{31}$ S/(S + R) (Figure 5d) and $C_{30}$ βα/(βα + αβ) (Figure 5e) values peak towards
379 higher thermal maturity during the core of the PETM, reaching a maximum of 0.38 and 0.04,
380 respectively. $C_{31}$ S/(S + R) values exhibit a drastic shift during the PETM (Fig. 5d) and there is
381 near equal mix of 22S and 22R isomers, suggesting potential transient input of thermally mature
382 organic carbon. Changes in the $C_{31}$ S/(S + R) ratio and $C_{30}$ βα/(βα + αβ) ratio does not occur
383 synchronously, instead $C_{31}$ S/(S + R) values lag behind by ~1.5 mcd.

384 3.1.5 TDP Site 14

385 $C_{16}$ to $C_{33}$ *n*-alkanes and $C_{27}$ to $C_{35}$ hopanes (including αβ, βα, and ββ isomers) were identified in
386 the apolar fraction. The CPI remains > 3 (i.e., low thermal maturity), with the exception of five
387 data points which occur during the core of the PETM (Figure 6b). Most noticeable is the large
388 variability in the hopane-based thermal maturity ratios pre-PETM and for the first ~4 m of the
389 core of the PETM. In the upper ~5 m of the core of the PETM, the ratios are more stable and in
390 general agreement. This interval mostly exhibits more thermally mature values than during the
391 pre-PETM section (e.g., $C_{31}$ αβ/(αβ + ββ) increases by an average of 0.5; Figure 6c), suggesting a
392 potential shift to an input of thermally mature organic carbon. For example, $C_{29\text{-}31}$ αβ/(αβ + ββ)
393 values are close to its mature endmember of 1 (Figure 6c).

394 3.2 $OC_{petro}$ mass accumulation rates

395 The $OC_{petro}$ MARs were acquired from all the sites and grouped (where possible) into the key
396 time intervals: (i) pre-PETM (Paleocene); (ii) the "core" (onset and body of the CIE) of the
397 PETM; (iii) the recovery of the PETM; (iiia) Phase I of the recovery, and (iiib) Phase II of the
398 recovery (see Text S1 in the supporting information). To enable comparison between sites, we
399 calculated the fold change in mean $OC_{petro}$ MARs between pre-PETM and during the PETM (i.e.,
400 including the core and recovery of the PETM) (Figure 7). Overall, most of the sites display an
401 increase in $OC_{petro}$ MARs during the PETM (ACEX: $7x10^{-2}$ gC $cm^2$ $kyr^{-1}$, Kheu River: $3x10^{-2}$
402 gC $cm^2$ $kyr^{-1}$, Ancora: $2x10^{-2}$ gC $cm^2$ $kyr^{-1}$, SDB: $6x10^{-2}$ gC $cm^2$ $kyr^{-1}$, CamDor: $8x10^{-3}$ gC $cm^2$

403 $kyr^{-1}$, TDP Site 14: and $8x10^{-3}$ gC $cm^2$ $kyr^{-1}$). However, the sites with the largest increase are
404 restricted to the mid-latitudes (i.e., Kheu River, Ancora, and SDB). In contrast, ODP Site 1172
405 exhibits a decrease ($3x10^{-4}$ gC $cm^2$ $kyr^{-1}$) in $OC_{petro}$ MAR during the PETM.

406 **4 Discussion**

407 4.1 Enhanced $OC_{petro}$ mass accumulation rates in the subtropics and mid-latitudes during
408 the PETM

409 A previous study from Tanzania (TDP Site 14) reported a relative increase in the thermally
410 mature αβ hopanes during the PETM (Carmichael et al., 2017; Handley et al., 2012). Here, we
411 present new hopane-based thermal maturity data that reveals rapidly fluctuating values within the
412 first ~4 m of the core of the PETM (Figure 6). Similar patterns were observed in the bulk $\delta^{13}C$ of
413 organic carbon ($\delta^{13}C_{org}$; Figure 6a), the *n*-alkane $\delta^{13}C$ record, the chain-length distributions of *n*-
414 alkanes, and the branched and isoprenoid tetraether (BIT) index (Figure S2 in the supporting
415 information; Aze et al., 2014; Carmichael et al., 2017; Handley et al., 2008, 2012). The $\delta^{13}C_{org}$
416 and *n*-alkane $\delta^{13}C$ records were previously suggested to reflect episodic reworking of older (pre-
417 PETM) material rather than changes in the atmospheric carbon reservoir (Figure 6 and S2 in the
418 supporting information; Aze et al., 2014; Handley et al., 2008). The hopane-based thermal
419 maturity ratios within this study confirms this variable delivery of $OC_{petro}$. In contrast, the upper
420 ~5 m of the core of the PETM exhibits more stability in the hopane-based thermal maturity ratios
421 (Carmichael et al., 2017; Handley et al., 2012), $\delta^{13}C_{org}$ values, and *n*-alkane $\delta^{13}C$ values (Aze et
422 al., 2014; Handley et al., 2008), indicating a switch from an episodic to persistent delivery of
423 $OC_{petro}$ (Carmichael et al., 2017; Handley et al., 2012). The hopane-based thermal maturity ratios
424 also indicate that the $OC_{petro}$ within this interval is of higher thermal maturity. During the PETM,
425 a rise in thermally mature hopanes and LSRs increases $OC_{petro}$ MARs by an average of $8x10^{-3}$ gC
426 $cm^2$ $kyr^{-1}$ (Figure 7). Enhanced $OC_{petro}$ MAR is consistent with a shift from predominantly
427 marine organic carbon to a terrestrial organic carbon source (e.g., an increase in the abundance of
428 long-chain *n*-alkanes produced by vascular plants and brGDGTs produced by soil bacteria;
429 Carmichael et al., 2017; Handley et al., 2008, 2012). Whilst there is greater LSR and terrigenous
430 sediment during the PETM, $C_{org}$ values declined. This drop was attributed to the larger
431 contribution of clay (Handley et al., 2012). Evidence includes an abundance of kaolinite,
432 suggestive of intensified physical erosion (John et al., 2012), and high Li/Al combined with low
433 Na/Al, suggestive of exhumation of older weathered clay. These additional proxies also indicate

processes that support an increase in the mobilisation and accumulation of $OC_{petro}$ during the PETM.

Similar to Tanzania, Ancora exhibits an increase in the average $OC_{petro}$ MARs (by $2x10^{-2}$ gC $cm^2$ $kyr^{-1}$) during the PETM. This value falls within the average $OC_{petro}$ MARs estimated at two other sites from the Atlantic Coastal Plain (i.e., $6x10^{-2}$ gC $cm^2$ $kyr^{-1}$ SDB and $8x10^{-3}$ gC $cm^2$ $kyr^{-1}$ CamDor; Figure 7). However, the higher $OC_{petro}$ MAR is largely driven by a shift in LSR from 0.8 cm $kyr^{-1}$ (pre-PETM) to 11.28 cm $kyr^{-1}$ (PETM) (Table 1; Stassen et al., 2012), and thus any uncertainty in the LSRs will also be reflected in the MAR estimates. The higher $OC_{petro}$ MAR is consistent with evidence of terrestrial input to the Atlantic Coastal Plain during the PETM, including a higher abundance of kaolinite (Gibson et al., 2000), detrital magnetic minerals (Kopp et al., 2009), charcoal, seed pods, and terrestrial spores (Self-Trail et al., 2017). In addition, there is an increase in the terrestrial aquatic ratio (TAR; Bourbonniere & Meyers, 1996; Lyons et al., 2019). Indirect evidence includes changes in the marine microfossil assemblage towards benthic foraminifera (Self-Trail et al., 2017) and dinoflagellates (Sluijs & Brinkhuis, 2009) that can tolerate brackish water with high sediment input (Self-Trail et al., 2017). However, with the exception of the abrupt peaks of $C_{31}$ S/(S + R) at ~169–171 mcd (Figure 5d) and $C_{30}$ βα/(βα + αβ) at ~171–173 mcd (Figure 5e), the thermal maturity ratios at Ancora are relatively stable compared to SDB and CamDor (Lyons et al., 2019). Unlike Ancora, SDB and CamDor are characterised by a 6 ‰ increase in $\delta^{13}C_{org}$ values during the PETM (Lyons et al., 2019), which was argued to represent reworking of older (pre-PETM) material and not an increase in primary production (Lyons et al., 2019). This $^{13}C$ enrichment is not observed at Ancora (Figure 5a; Elling et al., 2019) and is consistent with the relatively stable thermal maturity ratios during the PETM.

The average $OC_{petro}$ MARs at Kheu River exhibits an increase (by $3x10^{-2}$ gC $cm^2$ $kyr^{-1}$) during the PETM (Figure 7), driven by an order-of-magnitude rise in $C_{org}$ values from an average background level of ~0.1 wt. % (pre- and post-PETM) to ~4.4 wt. % (Dickson et al., 2014). However, in contrast to the sites discussed thus far, Kheu River thermal maturity ratios shift to immature values during the core of the PETM (Figure 4). During the PETM, the *n*-alkane distribution is dominated by long-chain homologues characteristic of vascular plants (Dickson et

al., 2014). It can therefore be argued that the shift observed in the thermal maturity ratios is mostly due to enhanced input of the $OC_{bio}$ (i.e., immature hopanes such as ββ isomers) transported from land, although in situ production cannot be dismissed. An increase in the Chemical Index of Alteration (CIA) and spike in Ti/Al during the PETM not only corroborates evidence for terrestrial input but possibly erosion of older (pre-PETM) material (Dickson et al., 2014). As such, both $OC_{petro}$ and (to a larger extent) $OC_{bio}$ were likely delivered to this site. $OC_{bio}$ burial may negate $CO_2$ released via enhanced $OC_{petro}$ oxidation (e.g., Bowen & Zachos, 2010; John et al., 2008; Kaya et al., 2022; Papadomanolaki et al., 2022; Sluijs, Röhl, et al., 2008). Therefore, understanding whether the Kheu River region was a net carbon source or sink requires further investigations, and this study highlights the need to quantify both $OC_{bio}$ and $OC_{petro}$ in marine sediments. Regardless, the subtropical and mid-latitude sites all exhibit an increase in $OC_{petro}$ MAR during the PETM, and thus suggest that $OC_{petro}$ oxidation may provide an additional source of $CO_2$.

4.2 Limited change in organic carbon sources in the high-latitudes during the PETM

In the subtropics and mid-latitudes, average $OC_{petro}$ MAR increased between $8x10^{-3}$ to $6x10^{-2}$ gC $cm^2$ $kyr^{-1}$ during the PETM for a given site (see Section 4.1). In the high-latitudes, $OC_{petro}$ MARs in the Arctic (ACEX) and the southwest Pacific Ocean (ODP Site 1172) either increase (by $7x10^{-2}$ gC $cm^2$ $kyr^{-1}$) or decrease (by $3x10^{-4}$ gC $cm^2$ $kyr^{-1}$), respectively (Figure 7). The decline observed at ODP Site 1172 is due to a small drop in $C_{org}$ values and LSRs. The marked rise at ACEX is mostly driven by a peak in TOC values, from a minimum of 1.3 % (pre-PETM) to a maximum of 4.9 % (core PETM) (Elling et al., 2019). Absolute abundances of palynomorphs from ACEX suggest that TOC is a mixture of marine and terrestrial organic matter (Sluijs, Röhl, et al., 2008). However, both sites, with the exception of the $C_{31}$ S/(S + R) ratio at ODP Site 1172 (Figure 3d), have stable thermal maturity ratios throughout the record. This indicates that although the supply of organic carbon increased during the PETM, the organic carbon source did not distinctly change. Intriguingly, there is an antiphase between $C_{30}$ αβ/(αβ + ββ) and $C_{31}$ αβ/(αβ + ββ) at ACEX (Figure 2c), perhaps suggesting subtle changes in the organic carbon source during the PETM. Decoupling between the $C_{30}$ and $C_{31}$ indices could be due to a greater input of acidic peats, which are dominated by $C_{31}$ αβ hopanes but lack abundant $C_{30}$ αβ isomers (Inglis et al., 2018). The contribution of $OC_{bio}$ from acidic peats at ACEX has also been inferred from brGDGTs (Sluijs et al., 2020).

### 4.3 Climate exerts primary control on $OC_{petro}$ mobilisation during the PETM

Various factors may explain why some shallow marine sediments are characterised by enhanced delivery of $OC_{petro}$ during the PETM. Modern observations have identified a strong link between rainfall and efficient erosion/transfer of organic carbon from land-to-sea (e.g., T. I. Eglinton et al., 2021; Hilton, 2017). In the subtropics, evidence for changes in the hydrological cycle during the PETM are scarce. Previous work at TDP Site 14 revealed that the hydrogen isotope of *n*-alkanes ($\delta^2H_{n\text{-alkanes}}$) increased during the PETM, which was inferred to represent a shift towards more arid climate conditions (Carmichael et al., 2017; Handley et al., 2008). Enhanced aridity could lead to minimal vegetation cover, hindering soil development, and maximising the potential for erosion and mobilisation of $OC_{petro}$ (e.g., Hilton et al., 2008; Leithold et al., 2006). Furthermore, there are large fluctuations in $\delta^2H_{n\text{-alkanes}}$ values, which may indicate oscillations between dry and wet climate states and/or an increase in extreme precipitation events (Carmichael et al., 2017; Handley et al., 2008). Modelling studies over subtropical Africa during the PETM support the latter (Carmichael et al., 2018). Episodic and intense rainfall on a landscape prone to erosion would explain the highly variable delivery of different organic carbon sources, as shown by the hopane-based thermal maturity data (this study), $\delta^{13}C_{org}$ values, and *n*-alkane $\delta^{13}C$ values (Aze et al., 2014; Handley et al., 2008).

Analogous to TDP Site 14, Kheu River also exhibits high variability in the thermal maturity ratios (e.g., CPI, $C_{29}$ αβ/$C_{30}$ αβ, and $C_{29}$ βα/(βα + αβ); Figure 4), chain-length distributions of *n*-alkanes, BIT index, grain-size, and CIA during the PETM (Dickson et al., 2014). Although two brief intervals of marine transgression have been noted in this region (Shcherbinina et al., 2016), the biomarker records are more variable and thus appear to be more consistent with episodic changes in precipitation. There are multiple lines of evidences associating other mid-latitude sites with increased transient and extreme rainfall events during the PETM. For example, the deposition of conglomerates in the Pyrenees (Chen et al., 2018; Schmitz & Pujalte, 2003, 2007) and changes in paleosol weathering indices and/or the abundance and composition of nodules in the Bighorn Basin (e.g., Kraus et al., 2013; Kraus & Riggins, 2007). There is also evidence for greater freshwater runoff in the Atlantic Coastal Plain (i.e., Ancora, SDB, and CamDor) during the PETM, with the development of a river-dominated shelf referred to as the "Appalachian Amazon" (Doubrawa et al., 2022; Kopp et al., 2009; Self-Trail et al., 2017). This is consistent

with high-resolution climate models that suggest the western Atlantic region was dominated by an increase in extratropical cyclones and more extreme rainfall events (Kiehl et al., 2021; Rush et al., 2021; Shields et al., 2021). Although the hydrological cycle likely exerted a first-order control on the mobilisation of terrestrial organic carbon, other ecological and/or geologic controls could have also been important. For example, the dominance of $OC_{bio}$ at Kheu River may reflect abundant vegetation cover (e.g., Goñi et al., 2013). On the other hand, the dominance of $OC_{petro}$ at TDP Site 14 may reflect greater availability of $OC_{petro}$-rich rock and/or exacerbated erosion of $OC_{petro}$ caused by limited soil and vegetation (e.g., Hilton et al., 2011).

Model simulations indicate an increase in precipitation in the high-latitudes for a PETM-type warming event (e.g., Carmichael et al., 2016; Cramwinckel et al., 2023; Winguth et al., 2010). Proxies also reconstruct northern and southern high-latitudes to be wetter at the onset of the PETM (e.g., evidence from palynomorphs (Korasidis et al., 2022; Sluijs et al., 2006; Willard et al., 2019), fossilised plants (Harding et al., 2011), hydrogen isotopes of *n*-alkanes ($\delta^2H_{n\text{-alkanes}}$; Pagani et al., 2006), and clay-mineralogy (Dypvik et al., 2011; Kaiho et al., 1996; Robert & Kennett, 1994)). Yet, biomarker evidence from high-latitude sites (i.e., ACEX and ODP Site 1172) indicates limited changes in the source of organic carbon during the PETM. This suggests that in order to exhume and mobilise $OC_{petro}$, changes in rainfall seasonality and frequency of extreme precipitation events may be required (see section 4.1). Alternatively, there may be other feedback mechanisms and/or more regional controls beyond the hydrological cycle. In modern systems, local geomorphic processes play a strong role in regulating $OC_{petro}$ transport from land-to-sea (e.g., Hilton & West, 2020). Variability in $OC_{petro}$ MARs could also be attributed to changes in sea level during the PETM. Indeed, various studies have suggested marine transgression during the PETM, including: ACEX (Sluijs et al., 2006); ODP Site 1172 (Sluijs et al., 2011); Kheu River (Shcherbinina et al., 2016); the Atlantic Coastal Plain (John et al., 2008); and elsewhere (Li et al., 2020; Jiang et al., 2023 and references therein; Sluijs, Brinkhuis, et al., 2008 and references therein). Although sea level rise is expected to reduce the supply of terrestrial organic carbon into the marine real, this is rarely observed (e.g., Sluijs et al., 2014) and most PETM sites are characterised by enhanced terrigenous material during the PETM (Carmichael et al., 2017 and references therein).

### 4.4 Timing and implications for $CO_2$ release during the PETM

Enhanced $OC_{petro}$ delivery was suggested to have occurred ~10–20 kyrs after the onset of the PETM (i.e., within the body of the CIE) by Lyons et al. (2019). Here, we confirm that elevated $OC_{petro}$ MARs occurred within the core of the PETM at several other sites (i.e., ACEX, Kheu River, Ancora; Figure 8). However, the exact timing within the core (i.e., onset or body) cannot be determined due to the lack of robust age constraints. The sites where the recovery phases were defined (i.e., ACEX, Kheu River, Ancora, and SDB), enables insight into whether enhanced $OC_{petro}$ MARs continued after the core interval or recovered to pre-PETM values. Interestingly, at both Ancora and SDB, median $OC_{petro}$ MARs are higher than the core of the PETM in Phase II and I, respectively (Figure 8). There is a decrease in $OC_{petro}$ MAR during Phase I of the recovery at Ancora, however this interval consists of a single data point. Although an increase in $OC_{petro}$ MAR during the recovery is not observed at ACEX and Kheu River, values do not return to pre-PETM levels. This suggests that at certain localities, terrestrial organic carbon cycle perturbations continued into the recovery phase. If $OC_{petro}$ was oxidised, it may have provided an additional source of $CO_2$ during the recovery. In this scenario, other negative feedback mechanisms are required to negate the additional carbon released and help assist in the recovery of the PETM. Several processes have been proposed, such as silicate weathering (Penman et al., 2014) and/or enhanced $OC_{bio}$ burial, either on land (Bowen, 2013; Bowen & Zachos, 2010) or within the ocean (John et al., 2008; Ma et al., 2014). For example, exacerbated weathering and erosion during the PETM (Pogge von Strandmann et al., 2021) may increase nutrient delivery from land-to-sea, stimulating primary productivity and therefore $OC_{bio}$ burial (Kaya et al., 2022; Papadomanolaki et al., 2022). However, the source of sequestered organic carbon in ocean sediments (i.e., terrestrial vs. marine) remains a major source of uncertainty.

Overall, Lyons et al. (2019) inferred between $10^2$ and $10^4$ PgC was released as $CO_2$ globally due to oxidation of $OC_{petro}$ during the PETM. This assumed that the three sites (i.e., SDB, CamDor, and TDP Site 14) are globally representative. However, this study demonstrates that enhanced $OC_{petro}$ MARs was mostly restricted to the subtropics and mid-latitudes, suggesting that global estimates may be lower than previously inferred. In addition, the maximum value of $10^4$ PgC assumed that 85% of $OC_{petro}$ is oxidised. However, increased erosion of clastic sediments can aid the preservation of $OC_{petro}$ (e.g., Bouchez et al., 2014; Burdige, 2007). Furthermore, intense

precipitation events (characteristic of the subtropics and mid-latitudes; e.g., Carmichael et al., 2017; Handley et al., 2008; Kiehl et al., 2021; Kraus et al., 2013; Kraus & Riggins, 2007; Rush et al., 2021; Schmitz & Pujalte, 2003, 2007; Shields et al., 2021) may reduce the transfer time of $OC_{petro}$ from source to sink, thereby reducing the possibility for oxidation (e.g., Hilton et al., 2011). However, it is important to consider that shallow marine sites will likely integrate an expansive catchment area, which incorporate slow meandering rivers as well as steep mountainous rivers. In the former system, the extent of $OC_{petro}$ oxidised could be as high as ~90 % (e.g., Bouchez et al., 2010; Galy et al., 2008). This is especially likely at sites where large freshwater input was evident, such as the Atlantic Coastal Plain (Doubrawa et al., 2022; Kopp et al., 2009; Self-Trail et al., 2017). We also demonstrate that $CO_2$ release may have continued into the recovery of the PETM, suggesting that other feedback mechanisms (e.g., $OC_{bio}$ burial) were necessary to aid in the recovery of the Earth's climate system. To constrain global estimates of $CO_2$ emitted from $OC_{petro}$ oxidation, future work is required to elucidate these uncertainties. For example, Raman spectroscopy could help identify the oxidation efficiency based on the degree of highly degradable vs. recalcitrant organic carbon (Sparkes et al., 2018) whilst paleo-digital elevation models may provide further insight on sediment routing systems and transit time during the PETM (Lyster et al., 2020).

## 5 Conclusion

This study uses a multi-biomarker approach to reconstruct the mobilisation of petrogenic organic carbon ($OC_{petro}$) during the PETM. We find widespread evidence for enhanced $OC_{petro}$ mass accumulation rates (MARs) in the subtropics and mid-latitudes during the PETM. In this region, we argue that extreme rainfall events exacerbated erosion, mobilisation, and burial of $OC_{petro}$ in the marine realm. In addition, we demonstrate that high $OC_{petro}$ MARs persisted into the recovery phase of the PETM. However, the high-latitude sites do not exhibit a distinct change in the source of organic carbon during the PETM. This may be due to a more stable hydrological regime and/or additional controls, such as geomorphic processes or sea level change. Overall, $OC_{petro}$ oxidation likely acted as an additional source of $CO_2$ during the PETM . However, further work is needed to determine the exact contributions of $OC_{petro}$ as a positive feedback mechanism during the PETM and other transient warming events.

**Acknowledgment**

G.N. Inglis is supported by a GCRF Royal Society Dorothy Hodgkin Fellowship (DHF\R1\191178) with additional support via the Royal Society (RF\ERE\231019, RF\ERE\210068). E.H. Hollingsworth acknowledges funding from a NERC (Grant NE/S007210). This research used samples provided by the Ocean Drilling Program (ODP) and the International Ocean Drilling Program (IODP). F.J. Elling is supported by Deutsche Forschungsgemeinschaft grant (441217575) and A. Pearson was supported by the US National Science Foundation (Grant OCE-1843285). We thank Katiana Doeana and Susan Carter at Havard University for laboratory assistance. For TDP Site 14 samples, we thank colleagues in the Tanzanian Drilling Project, and especially those from the Tanzanian Petroleum Development Corporation. Partial funding for M.P.S Badger was provided by NERC grant (NE/H006273/1). For Kheu River samples, we thank E.A. Shcherbinina, Y. Gavrilov, and A.J. Dickson who is supported by UKRI Frontier Research Grant (EP/X022080/1). We thank the NERC Life Sciences Mass Spectrometry Facility for technical support of the GC-MS and NERC for partial funding of the mass spectrometry facilities at Bristol (R8/H10/63. N.M. Papadomanolaki acknowledges funding from The Netherlands Earth System Science Center (NESSC), financially supported by the Ministry of Education, Culture and Science (OCW). We thank Arnold van Dijk for analytical assistance.

**Conflict of Interest**

The authors declare no conflicts of interest relevant to this study.

**Data Availability Statement**

The processed data used in this study are available at OSF and associated with a CC-By Attribution 4.0 International license (Hollingsworth, 2023).

**Author contributions:**

*Conceptualization*: E. H. Hollingsworth, G. N. Inglis

*Investigation*: E. H. Hollingsworth, F. J. Elling, M. P. S. Badger, A. J. Dickson, R. L. Rees-Owen, N. M. Papadomanolaki, G. N. Inglis

*Resources*: F. J. Elling, A. Pearson

*Visualisation*: E. H. Hollingsworth

*Writing* – original draft: E. H. Hollingsworth

*Writing* – review & editing: F. J. Elling, M. P. S. Badger, R. D. Pancost, A. J. Dickson, N. M. Papadomanolaki, A. Pearson, A. Sluijs, A. A. Baczynski, G. L. Foster, J. H. Whiteside, G. N. Inglis

*Project administration*: E. H. Hollingsworth, G. N. Inglis

*Supervision*: G. L. Foster, J. H. Whiteside, G. N. Inglis

**Figure captions**

**Figure 1:** Location of sites with new data (1-5) and published data (5-7). Paleogeographic reconstructions of 56 million years ago, adapted from Carmichael et al., (2017)

**Figure 2:** Thermal maturity ratios at ACEX. Note some of the axis (CPI and βα/(βα + αβ)) are reversed to reflect increasing thermal maturity towards the right. a) bulk sediment $\delta^{13}C$ of total organic carbon ($\delta^{13}C_{TOC}$) (Elling et al., 2019), b) CPI (this study), c) αβ/(αβ + ββ) ratios (this study), d) S/(S + R) ratio (this study), e) βα/(βα + αβ) ratio (this study), and f) $T_s/(T_s + T_m)$ ratio (this study). The PETM interval (including the core and recovery) is highlighted by grey shading, and a core gap is present from ~388 to 384.5 mcd (Sluijs et al., 2006)

**Figure 3:** Thermal maturity ratios at ODP Site 1172. Note some of the axis (CPI and βα/(βα + αβ)) are reversed to reflect increasing thermal maturity towards the right. a) bulk sediment $\delta^{13}C$ of total organic carbon ($\delta^{13}C_{TOC}$) (Sluijs et al., 2011), b) CPI (this study), c) αβ/(αβ + ββ) ratios (this study), d) S/(S + R) ratio (this study), and e) βα/(βα + αβ) ratio (this study). The PETM interval (including the core and recovery) is highlighted by grey shading

**Figure 4:** Thermal maturity ratios at Kheu River. Note some of the axis (CPI and βα/(βα + αβ)) are reversed to reflect increasing thermal maturity towards the right. a) bulk sediment $\delta^{13}C$ of organic carbon ($\delta^{13}C_{org}$) (Dickson et al., 2014), b) CPI (this study), c) αβ/(αβ + ββ) ratios (this study), d) $C_{29}$ αβ/$C_{30}$ αβ ratio (this study), e) βα/(βα + αβ) ratios (this study), and f) $T_s/(T_s + T_m)$ ratio (this study). The PETM interval (including the core and recovery) is highlighted by grey shading

**Figure 5:** Thermal maturity ratios at Ancora. Note some of the axis (CPI and βα/(βα + αβ)) are reversed to reflect increasing thermal maturity towards the right. a) bulk sediment $\delta^{13}C$ of total organic carbon ($\delta^{13}C_{TOC}$) (Elling et al., 2019), b) CPI (this study), c) αβ/(αβ + ββ) ratios (this

study), d) S/(S + R) ratio (this study), and e) βα/(βα + αβ) ratio (this study). The PETM interval (including the core and recovery) is highlighted by grey shading

**Figure 6:** Thermal maturity ratios at TDP Site 14. Note some of the axis (CPI and βα/(βα + αβ)) are reversed to reflect increasing thermal maturity towards the right. a) bulk sediment $\delta^{13}C$ of organic carbon ($\delta^{13}C_{org}$) (Aze et al., 2014), b) CPI (closed symbols from this study and open symbols from Handley et al., 2012), c) αβ/(αβ + ββ) ratios (closed symbols from this study and open symbols from Handley et al., 2012), d) S/(S + R) ratios (closed symbols from this study and open symbols from Handley et al., 2012), e) $C_{29}$ αβ/$C_{30}$ αβ ratio (Handley et al., 2012), and f) βα/(βα + αβ) ratios (Handley et al., 2012). The PETM interval (including the core) is highlighted by grey shading, and an unconformity truncates the CIE at 12.6 m

**Figure 7:** $Log_{10}$ fold change in mean $OC_{petro}$ mass accumulation rates (MARs) between pre-PETM and during the PETM (i.e., including the core and recovery of the PETM). The latitudes are defined as: high (> 60° N/S); mid- (30–60° N/S); and subtropics (15–30° N/S) (see Table S1 in the supporting information)

**Figure 8:** Violin plots of $OC_{petro}$ MARs (gC $cm^2$ $kyr^{-1}$) for the defined time intervals of sites with the recovery phase (a) ACEX, (b) Kheu River, (c) Ancora, and (d) SDB. The thick dashed line represents the median and the thin dashed line extends from the $25^{th}$ to $75^{th}$ percentiles. Note the discontinuous y-axis and two different scales of (b) Kheu River.

## References

Aze, T., Pearson, P. N., Dickson, A. J., Badger, M. P. S., Bown, P. R., Pancost, R. D., Gibbs, S. J., Huber, B. T., Leng, M. J., Coe, A. L., Cohen, A. S., & Foster, G. L. (2014). Extreme warming of tropical waters during the Paleocene – Eocene Thermal Maximum. *Geology*, *42*(9), 739–742. https://doi.org/10.1130/G35637.1

Berhe, A. A., Harte, J., Harden, J. W., & Torn, M. S. (2007). The Significance of the Erosion-induced Terrestrial Carbon Sink. *BioScience*, *57*(4), 337–346. https://doi.org/10.1641/B570408

Berner, R. A., & Caldeira, K. (1997). The need for mass balance and feedback in the geochemical carbon. *Geology*, *25*(10), 955–953. https://doi.org/10.1130/0091-7613(1997)025<0955

Berner, R. A., Lasaga, A. C., & Garrels, R. M. (1983). The carbonate-silicate geochemical cycle

and its effect on atmospheric carbon dioxide over the past 100 million years. *American Journal of Science*, *283*(7), 641–683. https://doi.org/10.2475/ajs.283.7.641

Bianchi, T. S., Cui, X., Blair, N. E., Burdige, D. J., Eglinton, T. I., & Galy, V. (2018). Centers of organic carbon burial and oxidation at the land-ocean interface. *Organic Geochemistry*, *115*, 138–155. https://doi.org/10.1016/j.orggeochem.2017.09.008

Blair, N. E., Leithold, E. L., Ford, S. T., Peeler, K. A., Holmes, J. C., & Perkey, D. W. (2003). The persistence of memory: The fate of ancient sedimentary organic carbon in a modern sedimentary system. *Geochimica et Cosmochimica Acta*, *67*(1), 63–73. https://doi.org/10.1016/S0016-7037(02)01043-8

Bolle, M. P., Pardo, A., Hinrichs, K. U., Adatte, T., Von Salis, K., Burns, S., Keller, G., & Muzylev, N. (2000). The Paleocene-Eocene transition in the marginal northeastern Tethys (Kazakhstan and Uzbekistan). *International Journal of Earth Sciences*, *89*(2), 390–414. https://doi.org/10.1007/s005310000092

Bouchez, J., Beyssac, O., Galy, V., Gaillardet, J., France-lanord, C., Maurice, L., & Moreira-turcq, P. (2010). Oxidation of petrogenic organic carbon in the Amazon floodplain as a source of atmospheric CO2. *Geology*, *38*(3), 255–258. https://doi.org/10.1130/G30608.1

Bouchez, J., Galy, V., Hilton, R. G., Gaillardet, J. Ô., Moreira-Turcq, P., Pérez, M. A., France-Lanord, C., & Maurice, L. (2014). Source, transport and fluxes of Amazon River particulate organic carbon: Insights from river sediment depth-profiles. *Geochimica et Cosmochimica Acta*, *133*, 280–298. https://doi.org/10.1016/j.gca.2014.02.032

Bourbonniere, R. A., & Meyers, P. A. (1996). Sedimentary geolipid records of historical changes in the watersheds and productivities of Lakes Ontario and Erie. *Limnology and Oceanography*, *41*(2), 352–359. https://doi.org/10.4319/lo.1996.41.2.0352

Bowen, G. J. (2013). Up in smoke: A role for organic carbon feedbacks in Paleogene hyperthermals. *Global and Planetary Change*, *109*, 18–29. https://doi.org/10.1016/j.gloplacha.2013.07.001

Bowen, G. J., Bralower, T. J., Delaney, M. L., Dickens, G. R., Kelly, D. C., Koch, P. L., Kump, L. R., Meng, J., Sloan, L. C., Thomas, E., Wing, S. L., & Zachos, J. C. (2006). Eocene hyperthermal event offers insight into greenhouse warming. *Eos*, *87*(17), 165–169. https://doi.org/10.1029/2006eo170002

Bowen, G. J., & Zachos, J. C. (2010). Rapid carbon sequestration at the termination of the

735 Palaeocene-Eocene Thermal Maximum. *Nature Geoscience*, *3*, 866–869.
736 https://doi.org/10.1038/ngeo1014
737 Bray, E. E., & Evans, E. D. (1961). Distribution of n-paraffins as a clue to recognition of source
738 beds. *Geochimica et Cosmochimica Acta*, *22*(1), 2–15. https://doi.org/10.1016/0016-
739 7037(61)90069-2
740 Burdige, D. J. (2007). Preservation of organic matter in marine sediments: Controls,
741 mechanisms, and an imbalance in sediment organic carbon budgets? *Chemical Reviews*,
742 *107*(2), 467–485. https://doi.org/10.1021/cr050347q
743 Bush, R. T., & McInerney, F. A. (2013). Leaf wax n-alkane distributions in and across modern
744 plants: Implications for paleoecology and chemotaxonomy. *Geochimica et Cosmochimica*
745 *Acta*, *117*, 161–179. https://doi.org/10.1016/j.gca.2013.04.016
746 Carmichael, M. J., Inglis, G. N., Badger, M. P. S., Naafs, B. D. A., Behrooz, L., Remmelzwaal,
747 S., Monteiro, F. M., Rohrssen, M., Farnsworth, A., Buss, H. L., Dickson, A. J., Valdes, P.
748 J., Lunt, D. J., & Pancost, R. D. (2017). Hydrological and associated biogeochemical
749 consequences of rapid global warming during the Paleocene-Eocene Thermal Maximum.
750 *Global and Planetary Change*, *157*, 114–138.
751 https://doi.org/10.1016/j.gloplacha.2017.07.014
752 Carmichael, M. J., Lunt, D. J., Huber, M., Heinemann, M., Kiehl, J., LeGrande, A., Loptson, C.
753 A., Roberts, C. D., Sagoo, N., Shields, C., Valdes, P. J., Winguth, A., Winguth, C., &
754 Pancost, R. D. (2016). A model-model and data-model comparison for the early Eocene
755 hydrological cycle. *Climate of the Past*, *12*(2), 455–481. https://doi.org/10.5194/cp-12-455-
756 2016
757 Carmichael, M. J., Pancost, R. D., & Lunt, D. J. (2018). Changes in the occurrence of extreme
758 precipitation events at the Paleocene – Eocene thermal maximum. *Earth and Planetary*
759 *Science Letters*, *501*, 24–36. https://doi.org/10.1016/j.epsl.2018.08.005
760 Chen, C., Guerit, L., Foreman, B. Z., Hassenruck-Gudipati, H. J., Adatte, T., Honegger, L.,
761 Perret, M., Sluijs, A., & Castelltort, S. (2018). Estimating regional flood discharge during
762 Palaeocene-Eocene global warming. *Scientific Reports*, *8*(1), 1–8.
763 https://doi.org/10.1038/s41598-018-31076-3
764 Clark, K. E., Hilton, R. G., West, A. J., Robles Caceres, A., Gröcke, D. R., Marthews, T. R.,
765 Ferguson, R. I., Asner, G. P., New, M., & Malhi, Y. (2017). Erosion of organic carbon from

766 the Andes and its effects on ecosystem carbon dioxide balance. *Journal of Geophysical*
767 *Research: Biogeosciences*, *122*(3), 449–469. https://doi.org/10.1002/2016JG003615
768 Clark, K. E., Stallard, R. F., Murphy, S. F., Scholl, M. A., González, G., Plante, A. F., &
769 McDowell, W. H. (2022). Extreme rainstorms drive exceptional organic carbon export from
770 forested humid-tropical rivers in Puerto Rico. *Nature Communications*, *13*(1), 1–8.
771 https://doi.org/10.1038/s41467-022-29618-5
772 Cramwinckel, M. J., Burls, N. J., Fahad, A. A., Knapp, S., West, C. K., Reichgelt, T.,
773 Greenwood, D. R., Chan, W. Le, Donnadieu, Y., Hutchinson, D. K., de Boer, A. M.,
774 Ladant, J. B., Morozova, P. A., Niezgodzki, I., Knorr, G., Steinig, S., Zhang, Z., Zhu, J.,
775 Feng, R., … Inglis, G. N. (2023). Global and Zonal-Mean Hydrological Response to Early
776 Eocene Warmth. *Paleoceanography and Paleoclimatology*, *38*(6), 1–21.
777 https://doi.org/10.1029/2022PA004542
778 Cui, Y., Diefendorf, A. F., Kump, L. R., Jiang, S., & Freeman, K. H. (2021). Synchronous
779 Marine and Terrestrial Carbon Cycle Perturbation in the High Arctic During the PETM.
780 *Paleoceanography and Paleoclimatology*, *36*(4), 1–21.
781 https://doi.org/10.1029/2020PA003942
782 Deconto, R. M., Galeotti, S., Pagani, M., Tracy, D., Schaefer, K., Zhang, T., Pollard, D., &
783 Beerling, D. J. (2012). Past extreme warming events linked to massive carbon release from
784 thawing permafrost. *Nature*, *484*(7392), 87–91. https://doi.org/10.1038/nature10929
785 Dickens, G. R. (2011). Down the Rabbit Hole: Toward appropriate discussion of methane release
786 from gas hydrate systems during the Paleocene-Eocene thermal maximum and other past
787 hyperthermal events. *Climate of the Past*, *7*(3), 831–846. https://doi.org/10.5194/cp-7-831-
788 2011
789 Dickens, G. R., Castillo, M. M., & Walker, J. C. G. (1997). A blast of gas in the latest Paleocene:
790 Simulating first-order effects of massive dissociation of oceanic methane hydrate. *Geology*,
791 *25*(3), 259–262. https://doi.org/10.1130/0091-7613(1997)025<0259:ABOGIT>2.3.CO;2
792 Dickens, G. R., O'Neil, J. R., Rea, D. K., & Owen, R. M. (1995). Dissociation of oceanic
793 methane hydrate as a cause of the carbon isotope excursion at the end of the Paleocene.
794 *Paleoceanography*, *10*(6), 965–971. https://doi.org/10.1029/95PA02087
795 Dickson, A. J., Rees-owen, R. L., März, C., Coe, A. L., Cohen, A. S., Pancost, R. D., Taylor, K.,
796 & Shcherbinina, E. (2014). The spread of marine anoxia on the northern Tethys margin

during the Paleocene-Eocene Thermal Maximum. *Paleoceanography*, *29*(6), 471–488. https://doi.org/10.1002/2014PA002629.Received

Diefendorf, A. F., & Freimuth, E. J. (2017). Extracting the most from terrestrial plant-derived n-alkyl lipids and their carbon isotopes from the sedimentary record: A review. *Organic Geochemistry*, *103*, 1–21. https://doi.org/10.1016/j.orggeochem.2016.10.016

Doubrawa, M., Stassen, P., Robinson, M. M., Babila, T. L., Zachos, J. C., & Speijer, R. P. (2022). Shelf Ecosystems Along the U.S. Atlantic Coastal Plain Prior to and During the Paleocene-Eocene Thermal Maximum: Insights Into the Stratigraphic Architecture. *Paleoceanography and Paleoclimatology*, *37*(10), 1–21. https://doi.org/10.1029/2022PA004475

Dunkley Jones, T., Manners, H.R., Hoggett, M., Kirtland Turner, S., Westerhold, T., Leng, M.J., Pancost, R.D., Ridgwell, A., Alegret, L., Duller, R. and Grimes, S.T., 2018. Dynamics of sediment flux to a bathyal continental margin section through the Paleocene–Eocene Thermal Maximum. *Climate of the Past*, *14*(7), pp.1035-1049.

Dypvik, H., Riber, L., Burca, F., Rüther, D., Jargvoll, D., Nagy, J., & Jochmann, M. (2011). The Paleocene-Eocene thermal maximum (PETM) in Svalbard - clay mineral and geochemical signals. *Palaeogeography, Palaeoclimatology, Palaeoecology*, *302*(3–4), 156–169. https://doi.org/10.1016/j.palaeo.2010.12.025

Eglinton, G., & Hamilton, R. J. (1967). Leaf epicuticular waxes. *Science*, *156*(3780), 1322–1335. https://doi.org/10.1126/science.156.3780.1322

Eglinton, T. I., Galy, V. V., Hemingway, J. D., Feng, X., Bao, H., Blattmann, T. M., Dickens, A. F., Gies, H., Giosan, L., Haghipour, N., Hou, P., Lupker, M., McIntyre, C. P., Montluçon, D. B., Peucker-Ehrenbrink, B., Ponton, C., Schefuß, E., Schwab, M. S., Voss, B. M., … Zhao, M. (2021). Climate control on terrestrial biospheric carbon turnover. *Proceedings of the National Academy of Sciences of the United States of America*, *118*(8). https://doi.org/10.1073/pnas.2011585118

Elling, F. J., Gottschalk, J., Doeana, K. D., Kusch, S., Hurley, S. J., & Pearson, A. (2019). Archaeal lipid biomarker constraints on the Paleocene-Eocene carbon isotope excursion. *Nature Communications*, *10*(1), 1–10. https://doi.org/10.1038/s41467-019-12553-3

Farrimond, P., Taylor, A., & Telnás, N. (1998). Biomarker maturity parameters : the role of generation and thermal degradation. *Organic Geochemistry*, *29*(5–7), 1181–1197.

https://doi.org/10.1016/S0146-6380(98)00079-5

French, K. L., Tosca, N. J., Cao, C., & Summons, R. E. (2012). Diagenetic and detrital origin of moretane anomalies through the Permian-Triassic boundary. *Geochimica et Cosmochimica Acta*, *84*, 104–125. https://doi.org/10.1016/j.gca.2012.01.004

Frieling, J., Svensen, H. H., Planke, S., Cramwinckel, M. J., Selnes, H., & Sluijs, A. (2016). Thermogenic methane release as a cause for the long duration of the PETM. *Proceedings of the National Academy of Sciences of the United States of America*, *113*(43), 12059–12064. https://doi.org/10.1073/pnas.1603348113

Galy, V., Beyssac, O., France-Lanord, C., & Eglinton, T. (2008). Recycling of Graphite During Himalayan Erosion: A Geological Stabilization of Carbon in the Crust. *Science*, *322*(5903), 943–945. https://doi.org/10.1126/science.1161408

Galy, V., France-Lanord, C., Beyssac, O., Faure, P., Kudrass, H., & Palhol, F. (2007). Efficient organic carbon burial in the Bengal fan sustained by the Himalayan erosional system. *Nature*, *450*(7168), 407–410. https://doi.org/10.1038/nature06273

Galy, V., Peucker-Ehrenbrink, B., & Eglinton, T. (2015). Global carbon export from the terrestrial biosphere controlled by erosion. *Nature*, *521*, 204–207. https://doi.org/10.1038/nature14400

Gibson, T. G., Bybell, L. M., & Mason, D. B. (2000). Stratigraphic and climatic implications of clay mineral changes around the Paleocene/Eocene boundary of the northeastern US margin. *Sedimentary Geology*, *134*(1–2), 65–92. https://doi.org/10.1016/S0037-0738(00)00014-2

Goñi, M. A., Hatten, J. A., Wheatcroft, R. A., & Borgeld, J. C. (2013). Particulate organic matter export by two contrasting small mountainous rivers from the Pacific Northwest, U.S.A. *Journal of Geophysical Research: Biogeosciences*, *118*(1), 112–134. https://doi.org/10.1002/jgrg.20024

Gutjahr, M., Ridgwell, A., Sexton, P. F., Anagnostou, E., Pearson, P. N., Pälike, H., Norris, R. D., Thomas, E., & Foster, G. L. (2017). Very large release of mostly volcanic carbon during the Palaeocene – Eocene Thermal Maximum. *Nature*, *548*, 573–577. https://doi.org/10.1038/nature23646

Handley, L., Crouch, E. M., & Pancost, R. D. (2011). A New Zealand record of sea level rise and environmental change during the Paleocene-Eocene Thermal Maximum. *Palaeogeography,*

*Palaeoclimatology, Palaeoecology*, *305*, 185–200. https://doi.org/10.1016/j.palaeo.2011.03.001

Handley, L., O'Halloran, A., Pearson, P. N., Hawkins, E., Nicholas, C. J., Schouten, S., McMillan, I. K., & Pancost, R. D. (2012). Changes in the hydrological cycle in tropical East Africa during the Paleocene-Eocene Thermal Maximum. *Palaeogeography, Palaeoclimatology, Palaeoecology*, *329–330*, 10–21. https://doi.org/10.1016/j.palaeo.2012.02.002

Handley, L., Pearson, P. N., Mcmillan, I. K., & Pancost, R. D. (2008). Large terrestrial and marine carbon and hydrogen isotope excursions in a new Paleocene/Eocene boundary section from Tanzania. *Earth and Planetary Science Letters*, *275*(1), 17–25. https://doi.org/10.1016/j.epsl.2008.07.030

Harding, I. C., Charles, A. J., Marshall, J. E. A., Pälike, H., Roberts, A. P., Wilson, P. A., Jarvis, E., Thorne, R., Morris, E., Moremon, R., Pearce, R. B., & Akbari, S. (2011). Sea-level and salinity fluctuations during the Paleocene-Eocene thermal maximum in Arctic Spitsbergen. *Earth and Planetary Science Letters*, *303*(1–2), 97–107. https://doi.org/10.1016/j.epsl.2010.12.043

Hilton, R. G. (2017). Climate regulates the erosional carbon export from the terrestrial biosphere. *Geomorphology*, *277*, 118–132. https://doi.org/10.1016/j.geomorph.2016.03.028

Hilton, R. G., Gaillardet, J., Calmels, D., & Birck, J. (2014). Geological respiration of a mountain belt revealed by the trace element rhenium. *Earth and Planetary Science Letters*, *403*, 27–36. https://doi.org/10.1016/j.epsl.2014.06.021

Hilton, R. G., Galy, A., & Hovius, N. (2008). Riverine particulate organic carbon from an active mountain belt: Importance of landslides. *Global Biogeochemical Cycles*, *22*(1), 1–12. https://doi.org/10.1029/2006GB002905

Hilton, R. G., Galy, A., Hovius, N., Horng, M., & Chen, H. (2011). Efficient transport of fossil organic carbon to the ocean by steep mountain rivers: An orogenic carbon sequestration mechanism. *Geology*, *39*(1), 71–74. https://doi.org/10.1130/G31352.1

Hilton, R. G., Galy, A., Hovius, N., Horng, M. J., & Chen, H. (2010). The isotopic composition of particulate organic carbon in mountain rivers of Taiwan. *Geochimica et Cosmochimica Acta*, *74*(11), 3164–3181. https://doi.org/10.1016/j.gca.2010.03.004

Hilton, R. G., Galy, V., Gaillardet, J., Dellinger, M., Bryant, C., O'Regan, M., Gröcke, D. R.,

Coxall, H., Bouchez, J., & Calmels, D. (2015). Erosion of organic carbon in the Arctic as a geological carbon dioxide sink. *Nature*, *524*, 84–87. https://doi.org/10.1038/nature14653

Hilton, R. G., & West, A. J. (2020). Mountains, erosion and the carbon cycle. *Nature Reviews Earth & Environment*, *1*, 284–299. https://doi.org/10.1038/s43017-020-0058-6

Hollingsworth, E. H. (2023). *Spatial and Temporal Patterns in Petrogenic Organic Carbon Mobilisation during the Paleocene-Eocene Thermal Maximum. [Dataset]*. https://doi.org/10.17605/OSF.IO/F8HJC

Inglis, G. N., Bragg, F., Burls, N. J., Cramwinckel, M. J., Evans, D., Foster, G. L., Huber, M., Lunt, D. J., Siler, N., Steinig, S., Tierney, J. E., Wilkinson, R., Anagnostou, E., de Boer, A. M., Dunkley Jones, T., Edgar, K. M., Hollis, C. J., Hutchinson, D. K., & Pancost, R. D. (2020). Global mean surface temperature and climate sensitivity of the early Eocene Climatic Optimum (EECO), Paleocene-Eocene Thermal Maximum (PETM), and latest Paleocene. *Climate of the Past*, *16*(5), 1953–1968. https://doi.org/10.5194/cp-16-1953-2020

Inglis, G. N., Naafs, B. D. A., Zheng, Y., McClymont, E. L., Evershed, R. P., & Pancost, R. D. (2018). Distributions of geohopanoids in peat: Implications for the use of hopanoid-based proxies in natural archives. *Geochimica et Cosmochimica Acta*, *224*, 249–261. https://doi.org/10.1016/j.gca.2017.12.029

Jiang, J., Hu, X., Li, J., Garzanti, E., Jiang, S., Cui, Y., & Wang, Y. (2023). Eustatic change across the Paleocene-Eocene Thermal Maximum in the epicontinental Tarim seaway. *Global and Planetary Change*, *229*(February), 104241. https://doi.org/10.1016/j.gloplacha.2023.104241

John, C. M., Banerjee, N. R., Longstaffe, F. J., Sica, C., Law, K. R., & Zachos, J. C. (2012). Clay assemblage and oxygen isotopic constraints on the weathering response to the Paleocene-Eocene thermal maximum, East Coast of North America. *Geology*, *40*(7), 591–594. https://doi.org/10.1130/G32785.1

John, C. M., Bohaty, S. M., Zachos, J. C., Sluijs, A., Gibbs, S., Brinkhuis, H., & Bralower, T. J. (2008). North American continental margin records of the Paleocene-Eocene thermal maximum: Implications for global carbon and hydrological cycling. *Paleoceanography*, *23*(2), 1–20. https://doi.org/10.1029/2007PA001465

Jones, M. T., Percival, L. M. E., Stokke, E. W., Frieling, J., Mather, T. A., Riber, L., Schubert, B. A., Schultz, B., Tegner, C., Planke, S., & Svensen, H. H. (2019). Mercury anomalies

921 across the Palaeocene-Eocene Thermal Maximum. *Climate of the Past*, *15*(1), 217–236.
922 https://doi.org/10.5194/cp-15-217-2019
923 Kaiho, K., Arinobu, T., Ishiwatari, R., Morgans, H. E. G., Okada, H., Takeda, N., Tazaki, K.,
924 Zhou, G., Kajiwara, Y., Matsumoto, R., Hirai, A., Niitsuma, N., & Wada, H. (1996). Latest
925 Paleocene benthic foraminferal extinction and environmental changes at Tawanui , New
926 Zealand. *Paleoceanography*, *11*(4), 447–465. https://doi.org/10.1029/96PA01021
927 Kao, S. J., Dai, M. H., Wei, K. Y., Blair, N. E., & Lyons, W. B. (2008). Enhanced supply of
928 fossil organic carbon to the Okinawa trough since the last deglaciation. *Paleoceanography*,
929 *23*(2), 1–10. https://doi.org/10.1029/2007PA001440
930 Kao, S. J., Hilton, R. G., Selvaraj, K., Dai, M., Zehetner, F., Huang, J. C., Hsu, S. C., Sparkes,
931 R., Liu, J. T., Lee, T. Y., Yang, J. Y. T., Galy, A., Xu, X., & Hovius, N. (2014).
932 Preservation of terrestrial organic carbon in marine sediments offshore Taiwan: Mountain
933 building and atmospheric carbon dioxide sequestration. *Earth Surface Dynamics*, *2*(1), 127–
934 139. https://doi.org/10.5194/esurf-2-127-2014
935 Kaya, M. Y., Dupont-Nivet, G., Frieling, J., Fioroni, C., Rohrmann, A., Altıner, S. Ö., Vardar,
936 E., Tanyaş, H., Mamtimin, M., & Zhaojie, G. (2022). The Eurasian epicontinental sea was
937 an important carbon sink during the Palaeocene-Eocene thermal maximum.
938 *Communications Earth and Environment*, *3*(1), 1–10. https://doi.org/10.1038/s43247-022-
939 00451-4
940 Kiehl, J. T., Zarzycki, C. M., Shields, C. A., & Rothstein, M. V. (2021). Simulated changes to
941 tropical cyclones across the Paleocene-Eocene Thermal Maximum (PETM) boundary.
942 *Palaeogeography, Palaeoclimatology, Palaeoecology*, *572*, 110421.
943 https://doi.org/10.1016/j.palaeo.2021.110421
944 Kirtland Turner, S. (2018). Constraints on the onset duration of the Paleocene-Eocene Thermal
945 Maximum. *Philosophical Transactions of the Royal Society A*, *376*(2130), 1–16.
946 https://doi.org/10.1098/rsta.2017.0082
947 Kopp, R. E., Schumann, D., Raub, T. D., Powars, D. S., Godfrey, L. V., Swanson-Hysell, N. L.,
948 Maloof, A. C., & Vali, H. (2009). An Appalachian Amazon? Magnetofossil evidence for the
949 development of a tropical river-like system in the mid-Atlantic United States during the
950 Paleocene-Eocene thermal maximum. *Paleoceanography*, *24*(4), 1–17.
951 https://doi.org/10.1029/2009PA001783

Korasidis, V. A., Wing, S. L., Shields, C. A., & Kiehl, J. T. (2022). Global Changes in Terrestrial Vegetation and Continental Climate During the Paleocene-Eocene Thermal Maximum. *Paleoceanography and Paleoclimatology*, *37*(4), 1–21. https://doi.org/10.1029/2021PA004325

Kraus, M. J., McInerney, F. A., Wing, S. L., Secord, R., Baczynski, A. A., & Bloch, J. I. (2013). Paleohydrologic response to continental warming during the Paleocene-Eocene Thermal Maximum, Bighorn Basin, Wyoming. *Palaeogeography, Palaeoclimatology, Palaeoecology*, *370*, 196–208. https://doi.org/10.1016/j.palaeo.2012.12.008

Kraus, M. J., & Riggins, S. (2007). Transient drying during the Paleocene-Eocene Thermal Maximum (PETM): Analysis of paleosols in the bighorn basin, Wyoming. *Palaeogeography, Palaeoclimatology, Palaeoecology*, *245*(3–4), 444–461. https://doi.org/10.1016/j.palaeo.2006.09.011

Kurtz, A. C., Kump, L. R., Arthur, M. A., Zachos, J. C., & Paytan, A. (2003). Early Cenozoic decoupling of the global carbon and sulfur cycles. *Paleoceanography*, *18*(4), 1–14. https://doi.org/10.1029/2003PA000908

Kusch, S., & Rush, D. (2022). Revisiting the precursors of the most abundant natural products on Earth: A look back at 30+ years of bacteriohopanepolyol (BHP) research and ahead to new frontiers. *Organic Geochemistry*, *172*, 104469. https://doi.org/10.1016/j.orggeochem.2022.104469

Lee, J.-Y., Marotzke, J., Bala, G., Cao, L., Corti, S., Dunne, J. P., Engelbrecht, F., Fischer, E., Fyfe, J. C., Jones, C., Maycock, A., Mutemi, J., Ndiaye, O., Panickal, S., & Zhou, T. (2021). Future Global Climate: Scenario-based Projections and Near-term Information Coordinating. In  and B. Z. Masson-Delmotte, V., P. Zhai, A. Pirani, S.L. Connors, C. Péan, S. Berger, N. Caud, Y. Chen, L. Goldfarb, M.I. Gomis, M. Huang, K. Leitzell, E. Lonnoy, J.B.R. Matthews, T.K. Maycock, T. Waterfield, O. Yelekçi, R. Yu (Ed.), *Climate Change 2021: The Physical Science Basis. Contribution of Working Group I to the Sixth Assessment Report of the Intergovernmental Panel on Climate Change*. Cambridge University Press. https://doi.org/10.1017/9781009157896.006.553

Leithold, E. L., Blair, N. E., & Perkey, D. W. (2006). Geomorphologic controls on the age of particulate organic carbon from small mountainous and upland rivers. *Global Biogeochemical Cycles*, *20*(3), 1–11. https://doi.org/10.1029/2005GB002677

Li, J., Hu, X., Zachos, J.C., Garzanti, E. and BouDagher-Fadel, M., 2020. Sea level, biotic and carbon-isotope response to the Paleocene–Eocene thermal maximum in Tibetan Himalayan platform carbonates. *Global and Planetary Change*, *194*, p.103316.

Lyons, S. L., Baczynski, A. A., Babila, T. L., Bralower, T. J., Hajek, E. A., Kump, L. R., Polites, E. G., Self-Trail, J. M., Trampush, S. M., Vornlocher, J. R., Zachos, J. C., & Freeman, K. H. (2019). Palaeocene–Eocene Thermal Maximum prolonged by fossil carbon oxidation. *Nature Geoscience*, *12*, 54–60. https://doi.org/10.1038/s41561-018-0277-3

Lyster, S. J., Whittaker, A. C., Allison, P. A., Lunt, D. J., & Farnsworth, A. (2020). Predicting sediment discharges and erosion rates in deep time—examples from the late Cretaceous North American continent. *Basin Research*, *32*(6), 1547–1573. https://doi.org/10.1111/bre.12442

Ma, Z., Gray, E., Thomas, E., Murphy, B., Zachos, J., & Paytan, A. (2014). Carbon sequestration during the Palaeocene-Eocene Thermal Maximum by an efficient biological pump. *Nature Geoscience*, *7*, 382–388. https://doi.org/10.1038/ngeo2139

Mackenzie, A. S., Patience, R. L., Maxwell, J. R., Vandenbroucke, M., & Durand, B. (1980). Molecular parameters of maturation in the Toarcian shales, Paris Basin, France—I. Changes in the configurations of acyclic isoprenoid alkanes, steranes and triterpanes. *Geochimica et Cosmochimica Acta*, *44*(11), 1709–1721. https://doi.org/10.1016/0016-7037(80)90222-7

McInerney, F. A., & Wing, S. L. (2011). The Paleocene-Eocene Thermal Maximum: A perturbation of carbon cycle, climate, and biosphere with implications for the future. *Annual Review of Earth and Planetary Sciences*, *39*, 489–516. https://doi.org/10.1146/annurev-earth-040610-133431

Meyers, S. R. (2014). *Astrochron: An R Package for Astrochronology https://cran.r-project.org/package=astrochron*.

Murphy, B. H., Farley, K. A., & Zachos, J. C. (2010). An extraterrestrial 3He-based timescale for the Paleocene-Eocene thermal maximum (PETM) from Walvis Ridge, IODP Site 1266. *Geochimica et Cosmochimica Acta*, *74*(17), 5098–5108. https://doi.org/10.1016/j.gca.2010.03.039

Pagani, M., Pedentchouk, N., Huber, M., Sluijs, A., Schouten, S., Brinkhuis, H., Dickens, G. R., Sinninghe Damsté, J. S., & Scientists, E. 302. (2006). Arctic hydrology during global warming at the Palaeocene / Eocene thermal maximum. *Nature*, *442*(7103), 671–675.

https://doi.org/10.1038/nature05043

Pancost, R. D., Coleman, J. M., Love, G. D., Chatzi, A., Bouloubassi, I., & Snape, C. E. (2008). Kerogen-bound glycerol dialkyl tetraether lipids released by hydropyrolysis of marine sediments: A bias against incorporation of sedimentary organisms? *Organic Geochemistry*, *39*(9), 1359–1371. https://doi.org/10.1016/j.orggeochem.2008.05.002

Papadomanolaki, N. M., Sluijs, A., & Slomp, C. P. (2022). Eutrophication and Deoxygenation Forcing of Marginal Marine Organic Carbon Burial During the PETM. *Paleoceanography and Paleoclimatology*, *37*(3), 1–23. https://doi.org/10.1029/2021PA004232

Penman, D. E., Hönisch, B., Zeebe, R. E., Thomas, E., & Zachos, J. C. (2014). Rapid and sustained surface ocean acidification during the Paleocene-Eocene Thermal Maximum. *Paleoceanography*, *29*(5), 357–369. https://doi.org/10.1002/2014PA002621

Peters, K. E., Walters, C. C., & Moldowan, J. M. (2005). *The Biomarker Guide Vols 1*. Cambridge University Press.

Petsch, S. T., Berner, R. A., & Eglinton, T. I. (2000). A field study of the chemical weathering of ancient sedimentary organic matter. *Organic Geochemistry*, *31*(5), 475–487. https://doi.org/10.1016/S0146-6380(00)00014-0

Pogge von Strandmann, P. A. E., Jones, M. T., Joshua West, A., Murphy, M. J., Stokke, E. W., Tarbuck, G., Wilson, D. J., Pearce, C. R., & Schmidt, D. N. (2021). Lithium isotope evidence for enhanced weathering and erosion during the Paleocene-Eocene Thermal Maximum. *Science Advances*, *7*(42), 1–12. https://doi.org/10.1126/sciadv.abh4224

Polik, C. A., Elling, F. J., & Pearson, A. (2018). Impacts of Paleoecology on the TEX 86 Sea Surface Temperature Proxy in the Pliocene-Pleistocene Mediterranean Sea. *Paleoceanography and Paleoclimatology*, *33*(12), 1472–1489. https://doi.org/10.1029/2018PA003494

Robert, C., & Kennett, J. P. (1994). Antarctic subtropical humid episode at the Paleocene-Eocene boundary: clay-mineral evidence. *Geology*, *22*(3), 211–214. https://doi.org/10.1130/0091-7613(1994)022<0211:ASHEAT>2.3.CO;2

Röhl, U., Westerhold, T., Bralower, T. J., & Zachos, J. C. (2007). On the duration of the Paleocene-Eocene thermal maximum (PETM). *Geochemistry, Geophysics, Geosystems*, *8*(12), 1–13. https://doi.org/10.1029/2007GC001784

Rosa-Putra, S., Nalin, R., Domenach, A. M., & Rohmer, M. (2001). Novel hopanoids from

Frankia spp. and related soil bacteria: Squalene cyclization and significance of geological biomarkers revisited. *European Journal of Biochemistry*, *268*(15), 4300–4306. https://doi.org/10.1046/j.1432-1327.2001.02348.x

Rush, W. D., Kiehl, J. T., Shields, C. A., & Zachos, J. C. (2021). Increased frequency of extreme precipitation events in the North Atlantic during the PETM: Observations and theory. *Palaeogeography, Palaeoclimatology, Palaeoecology*, *568*, 110289. https://doi.org/10.1016/j.palaeo.2021.110289

Schmitz, B., & Pujalte, V. (2003). Sea-level , humidity , and land-erosion records across the initial Eocene thermal maximum from a continental-marine transect in northern Spain. *Geology*, *31*(8), 689–692. https://doi.org/10.1130/G19527.1

Schmitz, B., & Pujalte, V. (2007). Abrupt increase in seasonal extreme precipitation at the Paleocene-Eocene boundary. *Geology*, *35*(3), 215–218. https://doi.org/10.1130/G23261A.1

Self-Trail, J. M., Robinson, M. M., Bralower, T. J., Sessa, J. A., Hajek, E. A., Kump, L. R., Trampush, S. M., Willard, D. A., Edwards, L. E., Powars, D. S., & Wandless, G. A. (2017). Shallow marine response to global climate change during the Paleocene-Eocene Thermal Maximum, Salisbury Embayment, USA. *Paleoceanography*, *32*(7), 710–728. https://doi.org/10.1002/2017PA003096

Shcherbinina, E., Gavrilov, Y., Iakovleva, A., Pokrovsky, B., Golovanova, O., & Aleksandrova, G. (2016). Environmental dynamics during the Paleocene-Eocene thermal maximum (PETM) in the northeastern Peri-Tethys revealed by high-resolution micropalaeontological and geochemical studies of a Caucasian key section. *Palaeogeography, Palaeoclimatology, Palaeoecology*, *456*, 60–81. https://doi.org/10.1016/j.palaeo.2016.05.006

Shields, C. A., Kiehl, J. T., Rush, W., Rothstein, M., & Snyder, M. A. (2021). Atmospheric rivers in high-resolution simulations of the Paleocene Eocene Thermal Maximum (PETM). *Palaeogeography, Palaeoclimatology, Palaeoecology*, *567*, 110293. https://doi.org/10.1016/j.palaeo.2021.110293

Sluijs, A., Bijl, P. K., Schouten, S., Röhl, U., Reichart, G.-J., & Brinkhuis, H. (2011). Southern ocean warming , sea level and hydrological change during the Paleocene-Eocene thermal maximum. *Climate of the Past*, *7*(1), 47–61. https://doi.org/10.5194/cp-7-47-2011

Sluijs, A., & Brinkhuis, H. (2009). A dynamic climate and ecosystem state during the Paleocene-Eocene Thermal Maximum: Inferences from dinoflagellate cyst assemblages on the New

Jersey Shelf. *Biogeosciences*, *6*(8), 1755–1781. https://doi.org/10.5194/bg-6-1755-2009

Sluijs, A., Brinkhuis, H., Crouch, E. M., John, C. M., Handley, L., Munsterman, D., Bohaty, S. M., Zachos, J. C., Reichart, G. J., Schouten, S., Pancost, R. D., Damsté, J. S. S., Welters, N. L. D., Lotter, A. F., & Dickens, G. R. (2008). Eustatic variations during the Paleocene-Eocene greenhouse world. *Paleoceanography*, *23*(4), 1–18. https://doi.org/10.1029/2008PA001615

Sluijs, A., Frieling, J., Inglis, G. N., Nierop, K. G. J., Peterse, F., Sangiorgi, F., & Schouten, S. (2020). Late Paleocene–early Eocene Arctic Ocean sea surface temperatures: reassessing biomarker paleothermometry at Lomonosov Ridge. *Climate of the Past*, *16*(6), 2381–2400. https://doi.org/10.5194/cp-16-2381-2020

Sluijs, A., Röhl, U., Schouten, S., Brumsack, H.-I., Sangiorgi, F., Sinninghe Damsté, J. S., & Brinkhuis, H. (2008). Arctic late Paleocene–early Eocene paleoenvironments with special emphasis on the Paleocene-Eocene thermal maximum (Lomonosov Ridge , Integrated Ocean Drilling Program Expedition 302). *Paleoceanography*, *23*(1), 1–17. https://doi.org/10.1029/2007PA001495

Sluijs, A., Schouten, S., Pagani, M., Woltering, M., Brinkhuis, H., Dickens, G. R., Huber, M., Reichart, G., Stein, R., Matthiessen, J., Lourens, L. J., Pedentchouk, N., Backman, J., & Moran, K. (2006). Subtropical Arctic Ocean temperatures during the Palaeocene/Eocene thermal maximum. *Nature*, *441*(1), 610–613. https://doi.org/10.1038/nature04668

Sluijs, A., van Roij, L., Harrington, G. J., Schouten, S., Sessa, J. A., Levay, L. J., Reichart, G.-J., & Slomp, C. P. (2014). Warming , euxinia and sea level rise during the Paleocene-Eocene Thermal Maximum on the Gulf Coastal Plain: implications for ocean oxygenation and nutrient cycling. *Climate of the Past*, *10*(4), 1421–1439. https://doi.org/10.5194/cp-10-1421-2014

Smith, J. C., Galy, A., Hovius, N., Tye, A. M., Turowski, J. M., & Schleppi, P. (2013). Runoff-driven export of particulate organic carbon from soil in temperate forested uplands. *Earth and Planetary Science Letters*, *365*, 198–208. https://doi.org/10.1016/j.epsl.2013.01.027

Sparkes, R. B., Maher, M., Blewett, J., Selver, A. O., Gustafsson, O., Semiletov, I. P., & Van Dongen, B. E. (2018). Carbonaceous material export from Siberian permafrost tracked across the Arctic Shelf using Raman spectroscopy. *Cryosphere*, *12*, 3293–3309. https://doi.org/10.5194/tc-12-3293-2018

1107 Stallard, R. F. (1998). Terrestrial sedimentation and the carbon cycle: Coupling weathering and
1108 erosion to carbon burial. *Global Biogeochemical Cycles*, *12*(2), 231–257.
1109 https://doi.org/10.1029/98GB00741
1110 Stassen, P., Thomas, E., & Speijer, R. P. (2012). Integrated stratigraphy of the Paleocene-Eocene
1111 thermal maximum in the New Jersey Coastal Plain: Toward understanding the effects of
1112 global warming in a shelf environment. *Paleoceanography*, *27*(4), 1–17.
1113 https://doi.org/10.1029/2012PA002323
1114 Storey, M., Duncan, R. A., & Swisher, C. C. (2007). Paleocene-Eocene thermal maximum and
1115 the opening of the northeast Atlantic. *Science*, *316*(5824), 587–589.
1116 https://doi.org/10.1126/science.1135274
1117 Svensen, H., Planke, S., Maithe-Sørensen, A., Jamtveit, B., Myklebust, R., Eidem, T. R., & Rey,
1118 S. S. (2004). Release of methane from a volcanic basin as a mechanism for initial Eocene
1119 global warming. *Nature*, *429*, 542–545. https://doi.org/10.1038/nature02566
1120 Tierney, J. E., Zhu, J., Li, M., Ridgwell, A., Hakim, G. J., Poulsen, C. J., Whiteford, R. D. M.,
1121 Rae, J. W. B., & Kump, L. R. (2022). Spatial patterns of climate change across the
1122 Paleocene–Eocene Thermal Maximum. *Proceedings of the National Academy of Sciences of*
1123 *the United States of America*, *119*(42), 1–7. https://doi.org/10.1073/pnas.2205326119
1124 Walker, J. C. G., Hays, P. B., & Kasting, J. F. (1981). A Negative Feedback Mechanism for the
1125 Long-term Stabilization of Earth's Surface Temperature. *Journal of Geophysical Research*,
1126 *86*(10), 9776–9782. https://doi.org/10.1029/JC086iC10p09776
1127 Willard, D. A., Donders, T. H., Reichgelt, T., Greenwood, D. R., Sangiorgi, F., Peterse, F.,
1128 Nierop, K. G. J., Frieling, J., & Schouten, S. (2019). Arctic vegetation , temperature , and
1129 hydrology during Early Eocene transient global warming events. *Global and Planetary*
1130 *Change*, *178*, 139–152. https://doi.org/10.1016/j.gloplacha.2019.04.012
1131 Winguth, A., Shellito, C., Shields, C., & Winguth, C. (2010). Climate response at the paleocene-
1132 eocene thermal maximum to greenhouse gas forcing-a model study with CCSM3. *Journal*
1133 *of Climate*, *23*(10), 2562–2584. https://doi.org/10.1175/2009JCLI3113.1
1134 Zeebe, R. E. (2013). What caused the long duration of the Paleocene-Eocene Thermal
1135 Maximum. *Paleoceanography*, *28*(3), 440–452. https://doi.org/10.1002/palo.20039
1136 Zeebe, R. E., Dickens, G. R., Ridgwell, A., Sluijs, A., & Thomas, E. (2014). Onset of carbon
1137 isotope excursion at the Paleocene-Eocene thermal maximum took millennia, not 13 years.

*Proceedings of the National Academy of Sciences of the United States of America*, *111*(12), 1062–1063. https://doi.org/10.1073/pnas.1321177111

Zeebe, R. E., & Lourens, L. J. (2019). Solar System chaos and the Paleocene–Eocene boundary age constrained by geology and astronomy. *Science*, *929*(6456), 926–929. https://doi.org/10.1126/science.aax0612

Zeebe, R. E., Zachos, J. C., & Dickens, G. R. (2009). Carbon dioxide forcing alone insufficient to explain Palaeocene-Eocene Thermal Maximum warming. *Nature Geoscience*, *2*, 576–580. https://doi.org/10.1038/ngeo578

## References from the Supporting Information

Aze, T., Pearson, P. N., Dickson, A. J., Badger, M. P. S., Bown, P. R., Pancost, R. D., Gibbs, S. J., Huber, B. T., Leng, M. J., Coe, A. L., Cohen, A. S., & Foster, G. L. (2014). Extreme warming of tropical waters during the Paleocene – Eocene Thermal Maximum. *Geology*, *42*(9), 739–742. https://doi.org/10.1130/G35637.1

Bolle, M. P., Pardo, A., Hinrichs, K. U., Adatte, T., Von Salis, K., Burns, S., Keller, G., & Muzylev, N. (2000). The Paleocene-Eocene transition in the marginal northeastern Tethys (Kazakhstan and Uzbekistan). *International Journal of Earth Sciences*, *89*(2), 390–414. https://doi.org/10.1007/s005310000092

Bralower, T. J., Kump, L. R., Self-Trail, J. M., Robinson, M. M., Lyons, S., Babila, T., Ballaron, E., Freeman, K. H., Hajek, E., Rush, W., & Zachos, J. C. (2018). Evidence for Shelf Acidification During the Onset of the Paleocene-Eocene Thermal Maximum. *Paleoceanography and Paleoclimatology*, *33*(12), 1408–1426. https://doi.org/10.1029/2018PA003382

Carmichael, M. J., Inglis, G. N., Badger, M. P. S., Naafs, B. D. A., Behrooz, L., Remmelzwaal, S., Monteiro, F. M., Rohrssen, M., Farnsworth, A., Buss, H. L., Dickson, A. J., Valdes, P. J., Lunt, D. J., & Pancost, R. D. (2017). Hydrological and associated biogeochemical consequences of rapid global warming during the Paleocene-Eocene Thermal Maximum. *Global and Planetary Change*, *157*, 114–138. https://doi.org/10.1016/j.gloplacha.2017.07.014

Dickson, A. J., Rees-owen, R. L., März, C., Coe, A. L., Cohen, A. S., Pancost, R. D., Taylor, K.,

& Shcherbinina, E. (2014). The spread of marine anoxia on the northern Tethys margin during the Paleocene-Eocene Thermal Maximum. *Paleoceanography*, *29*(6), 471–488. https://doi.org/10.1002/2014PA002629.Received

Doubrawa, M., Stassen, P., Robinson, M. M., Babila, T. L., Zachos, J. C., & Speijer, R. P. (2022). Shelf Ecosystems Along the U.S. Atlantic Coastal Plain Prior to and During the Paleocene-Eocene Thermal Maximum: Insights Into the Stratigraphic Architecture. *Paleoceanography and Paleoclimatology*, *37*(10), 1–21. https://doi.org/10.1029/2022PA004475

Elling, F. J., Gottschalk, J., Doeana, K. D., Kusch, S., Hurley, S. J., & Pearson, A. (2019). Archaeal lipid biomarker constraints on the Paleocene-Eocene carbon isotope excursion. *Nature Communications*, *10*(1), 1–10. https://doi.org/10.1038/s41467-019-12553-3

Gavrilov, Y. O., Shcherbinina, E. A., & Oberhänsli, H. (2003). Paleocene-Eocene boundary events in the northeastern Peri-Tethys. *Special Paper of the Geological Society of America*, *369*, 147–168. https://doi.org/10.1130/0-8137-2369-8.147

Handley, L., O'Halloran, A., Pearson, P. N., Hawkins, E., Nicholas, C. J., Schouten, S., McMillan, I. K., & Pancost, R. D. (2012). Changes in the hydrological cycle in tropical East Africa during the Paleocene-Eocene Thermal Maximum. *Palaeogeography, Palaeoclimatology, Palaeoecology*, *329–330*, 10–21. https://doi.org/10.1016/j.palaeo.2012.02.002

Handley, L., Pearson, P. N., Mcmillan, I. K., & Pancost, R. D. (2008). Large terrestrial and marine carbon and hydrogen isotope excursions in a new Paleocene/Eocene boundary section from Tanzania. *Earth and Planetary Science Letters*, *275*(1), 17–25. https://doi.org/10.1016/j.epsl.2008.07.030

Harris, A. D., Miller, K. G., Browning, J. V., Sugarman, P. J., Olsson, R. K., Cramer, B. S., & Wright, J. D. (2010). Integrated stratigraphic studies of Paleocene-lowermost Eocene sequences, New Jersey Coastal Plain: Evidence for glacioeustatic control. *Paleoceanography*, *25*(3), 1–18. https://doi.org/10.1029/2009PA001800

Hollis, C. J., Dunkley Jones, T., Anagnostou, E., Bijl, P. K., Cramwinckel, M. J., Cui, Y., Dickens, G. R., Edgar, K. M., Eley, Y., Evans, D., Foster, G. L., Frieling, J., Inglis, G. N., Kennedy, E. M., Kozdon, R., Lauretano, V., Lear, C. H., Littler, K., Lourens, L., … Lunt, D. J. (2019). The DeepMIP contribution to PMIP4: Methodologies for selection,

compilation and analysis of latest Paleocene and early Eocene climate proxy data, incorporating version 0.1 of the DeepMIP database. *Geoscientific Model Development*, *12*(7), 3149–3206. https://doi.org/10.5194/gmd-12-3149-2019

John, C. M., Bohaty, S. M., Zachos, J. C., Sluijs, A., Gibbs, S., Brinkhuis, H., & Bralower, T. J. (2008). North American continental margin records of the Paleocene-Eocene thermal maximum: Implications for global carbon and hydrological cycling. *Paleoceanography*, *23*(2), 1–20. https://doi.org/10.1029/2007PA001465

Junium, C. K., Dickson, A. J., & Uveges, B. T. (2018). Perturbation to the nitrogen cycle during rapid Early Eocene global warming. *Nature Communications*, *9*(1). https://doi.org/10.1038/s41467-018-05486-w

Lyons, S. L., Baczynski, A. A., Babila, T. L., Bralower, T. J., Hajek, E. A., Kump, L. R., Polites, E. G., Self-Trail, J. M., Trampush, S. M., Vornlocher, J. R., Zachos, J. C., & Freeman, K. H. (2019). Palaeocene–Eocene Thermal Maximum prolonged by fossil carbon oxidation. *Nature Geoscience*, *12*, 54–60. https://doi.org/10.1038/s41561-018-0277-3

Nicholas, C. J., Pearson, P. N., Bown, P. R., Jones, T. D., Huber, B. T., Karega, A., Lees, J. A., McMillan, I. K., O'Halloran, A., Singano, J. M., & Wade, B. S. (2006). Stratigraphy and sedimentology of the Upper Cretaceous to Paleogene Kilwa Group, southern coastal Tanzania. Journal of African Earth Sciences, 45, 431–466. https://doi.org/10.1016/j.jafrearsci.2006.04.003

Self-Trail, J. M., Powars, D. S., Watkins, D. K., & Wandless, G. A. (2012). Calcareous nannofossil assemblage changes across the Paleocene-Eocene Thermal Maximum: Evidence from a shelf setting. *Marine Micropaleontology*, *92–93*, 61–80. https://doi.org/10.1016/j.marmicro.2012.05.003

Shcherbinina, E., Gavrilov, Y., Iakovleva, A., Pokrovsky, B., Golovanova, O., & Aleksandrova, G. (2016). Environmental dynamics during the Paleocene-Eocene thermal maximum (PETM) in the northeastern Peri-Tethys revealed by high-resolution micropalaeontological and geochemical studies of a Caucasian key section. *Palaeogeography, Palaeoclimatology, Palaeoecology*, *456*, 60–81. https://doi.org/10.1016/j.palaeo.2016.05.006

Sluijs, A., Bijl, P. K., Schouten, S., Röhl, U., Reichart, G.-J., & Brinkhuis, H. (2011). Southern ocean warming , sea level and hydrological change during the Paleocene-Eocene thermal maximum. *Climate of the Past*, *7*(1), 47–61. https://doi.org/10.5194/cp-7-47-2011

1230 Sluijs, A., Röhl, U., Schouten, S., Brumsack, H.-I., Sangiorgi, F., Sinninghe Damsté, J. S., &
1231 Brinkhuis, H. (2008). Arctic late Paleocene–early Eocene paleoenvironments with special
1232 emphasis on the Paleocene-Eocene thermal maximum (Lomonosov Ridge , Integrated
1233 Ocean Drilling Program Expedition 302). *Paleoceanography*, *23*(1), 1–17.
1234 https://doi.org/10.1029/2007PA001495
1235 Sluijs, A., Schouten, S., Pagani, M., Woltering, M., Brinkhuis, H., Dickens, G. R., Huber, M.,
1236 Reichart, G., Stein, R., Matthiessen, J., Lourens, L. J., Pedentchouk, N., Backman, J., &
1237 Moran, K. (2006). Subtropical Arctic Ocean temperatures during the Palaeocene/Eocene
1238 thermal maximum. *Nature*, *441*(1), 610–613. https://doi.org/10.1038/nature04668
1239 Stassen, P., Thomas, E., & Speijer, R. P. (2012). Integrated stratigraphy of the Paleocene-Eocene
1240 thermal maximum in the New Jersey Coastal Plain: Toward understanding the effects of
1241 global warming in a shelf environment. *Paleoceanography*, *27*(4), 1–17.
1242 https://doi.org/10.1029/2012PA002323

**Figure 1.**

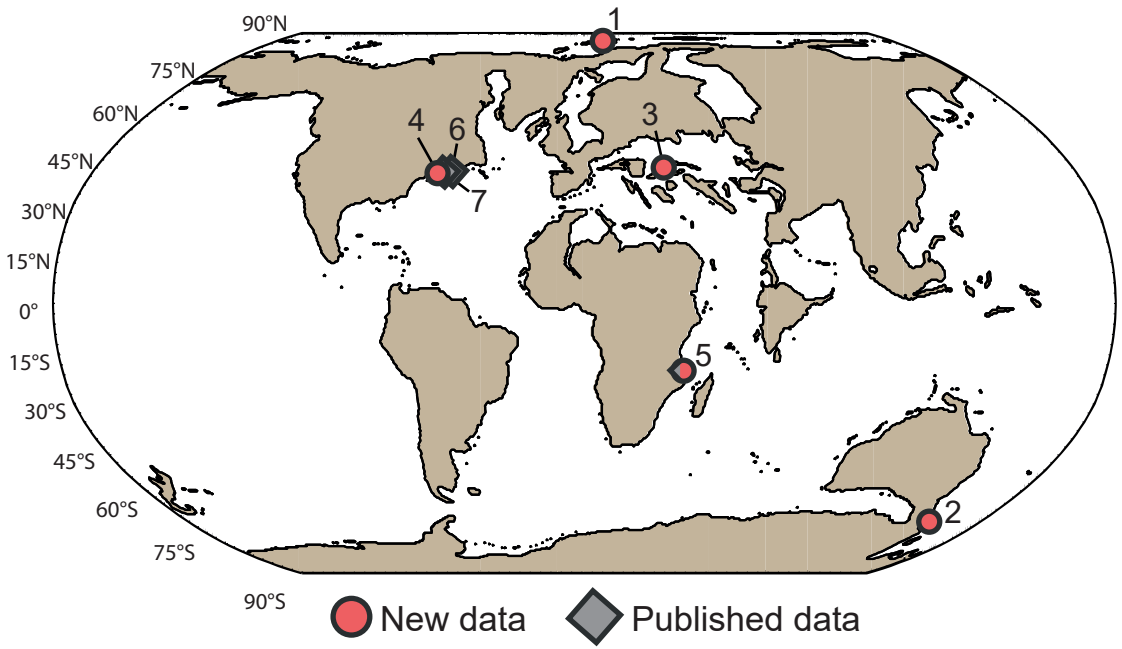


1. ACEX
2. ODP Site 1172
3. Kheu River
4. Ancora
5. TDP Site 14
6. SDB
7. CamDor

**Figure 2.**

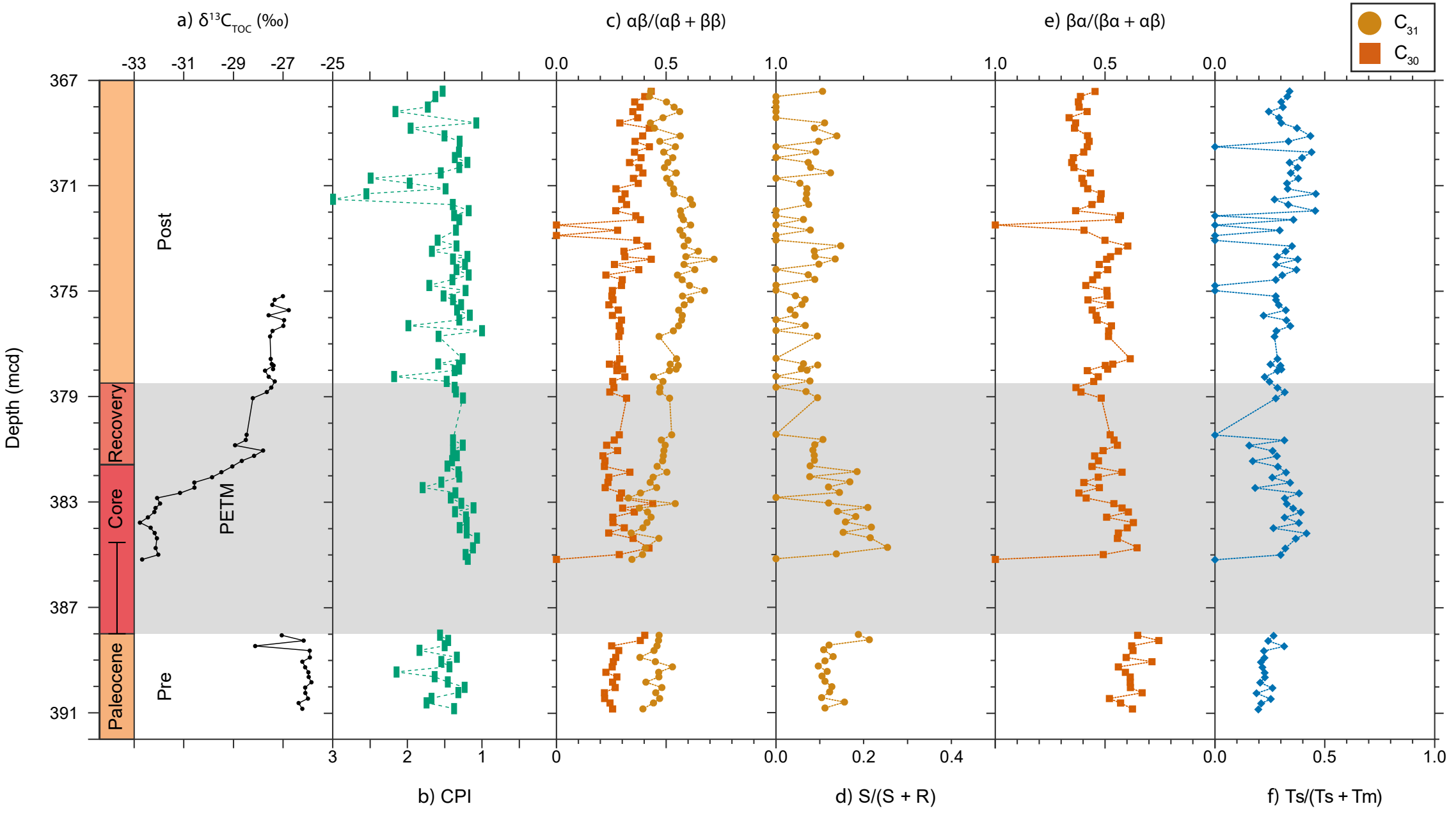
a) δ13CTOC (‰)
c) αβ/(αβ + ββ)
e) βα/(βα + αβ)
C31
C30
-33
-31
-29
-27
-25
0.0
0.5
1.0
1.0
0.5
0.0
Depth (mcd)
367
371
375
379
383
387
391
Post
Recovery
Core
Paleocene
Pre
PETM
3
2
1
0
0.0
0.2
0.4
0.0
0.5
1.0
b) CPI
d) S/(S + R)
f) Ts/(Ts + Tm)

**Figure 3.**

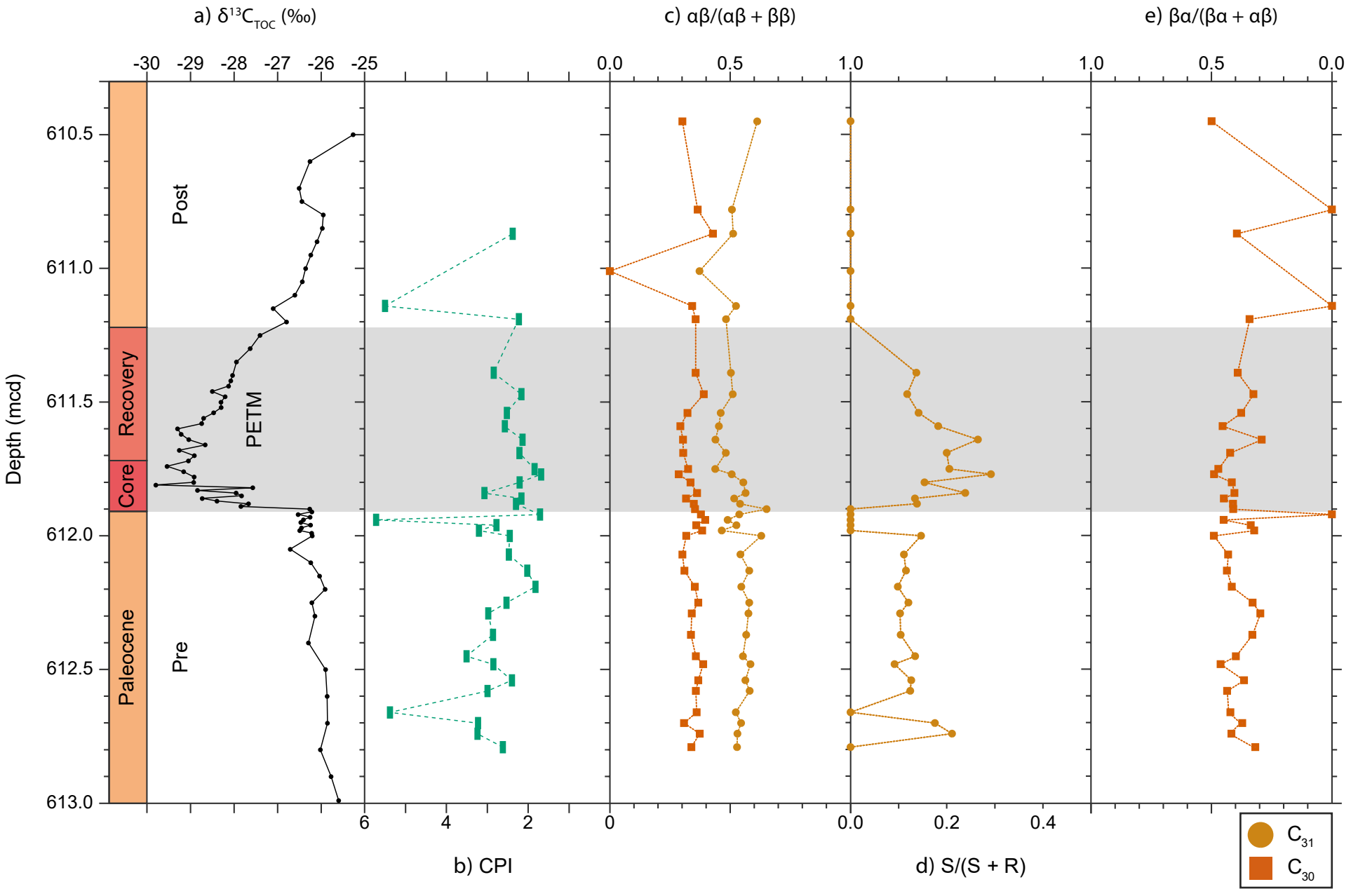
a) δ13CTOC (‰)
-30
-29
-28
-27
-26
-25
b) CPI
6
4
2
c) αβ/(αβ + ββ)
0.0
0.5
1.0
0
d) S/(S + R)
0.0
0.2
0.4
e) βα/(βα + αβ)
1.0
0.5
0.0
Depth (mcd)
610.5
611.0
611.5
612.0
612.5
613.0
Post
PETM
Pre
Recovery
Core
Paleocene
C31
C30

**Figure 4.**

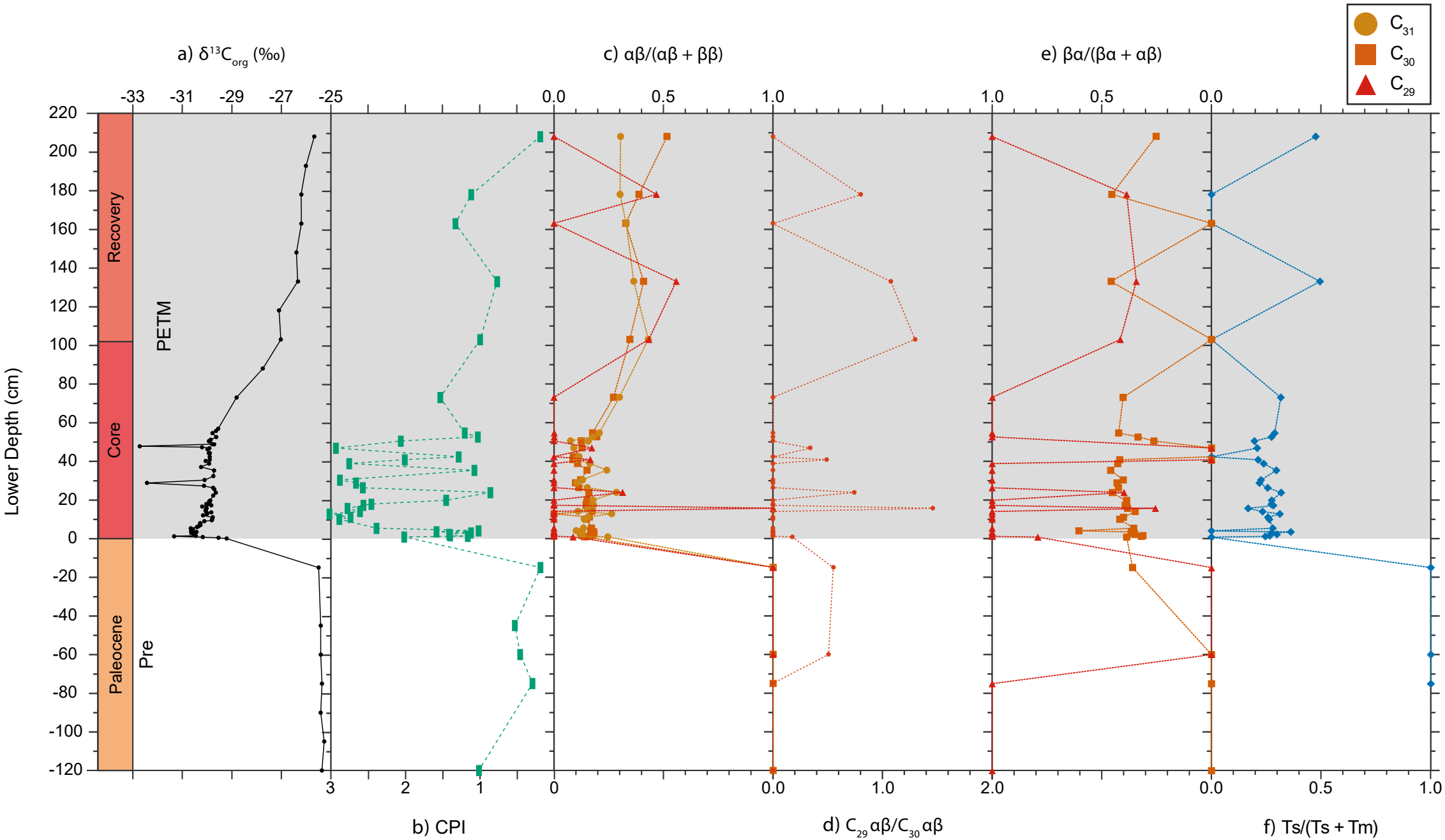
a) δ13Corg (‰)
c) αβ/(αβ + ββ)
e) βα/(βα + αβ)
C31
C30
C29
Lower Depth (cm)
Recovery
Core
Paleocene
PETM
Pre
b) CPI
d) C29αβ/C30αβ
f) Ts/(Ts + Tm)

**Figure 5.**

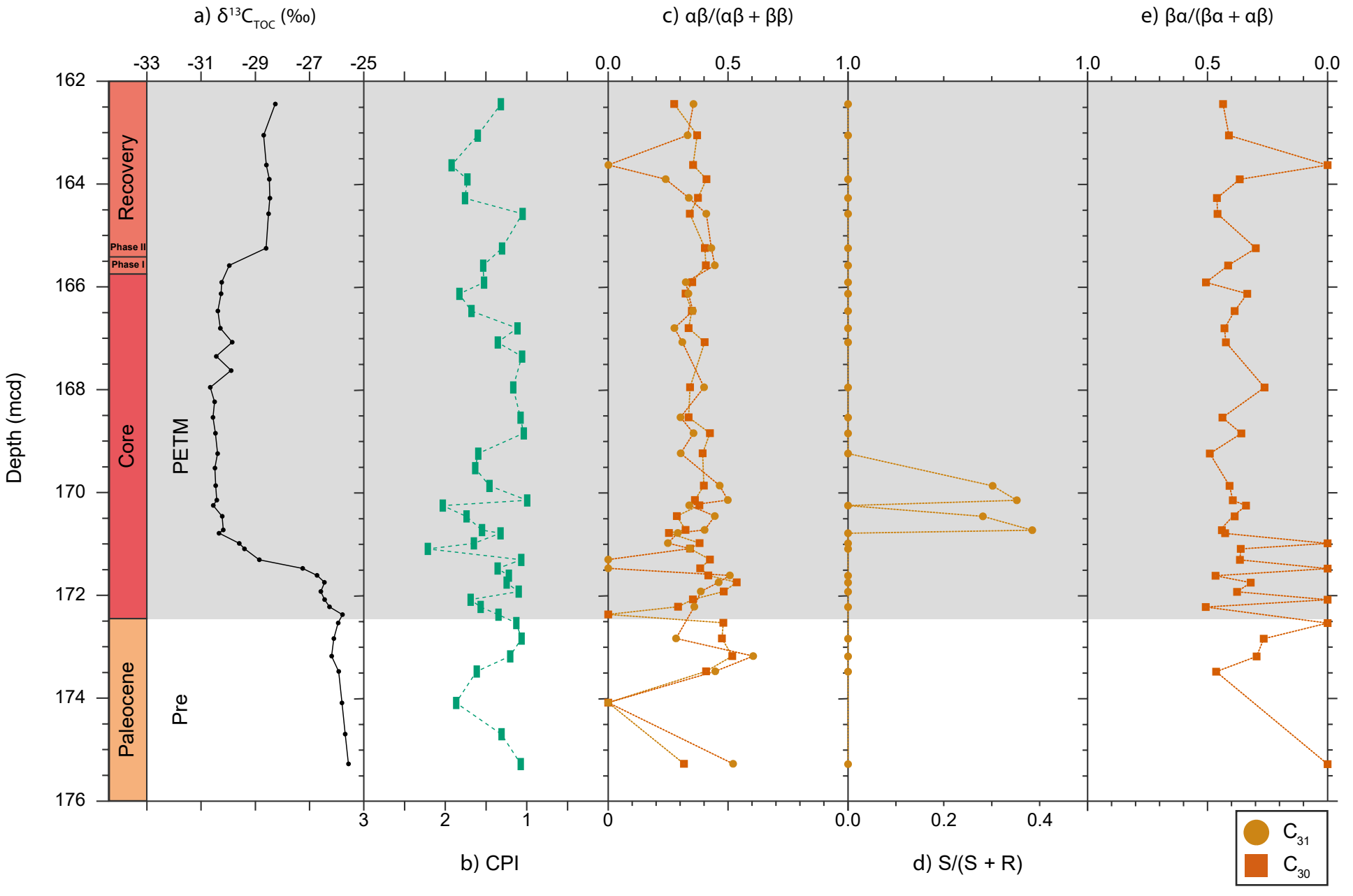
a) δ13CTOC (‰)
c) αβ/(αβ + ββ)
e) βα/(βα + αβ)
-33
-31
-29
-27
-25
0.0
0.5
1.0
1.0
0.5
0.0
Depth (mcd)
162
164
166
168
170
172
174
176
Recovery
Phase II
Phase I
Core
Paleocene
PETM
Pre
3
2
1
0
0.0
0.2
0.4
b) CPI
d) S/(S + R)
C31
C30

**Figure 6.**

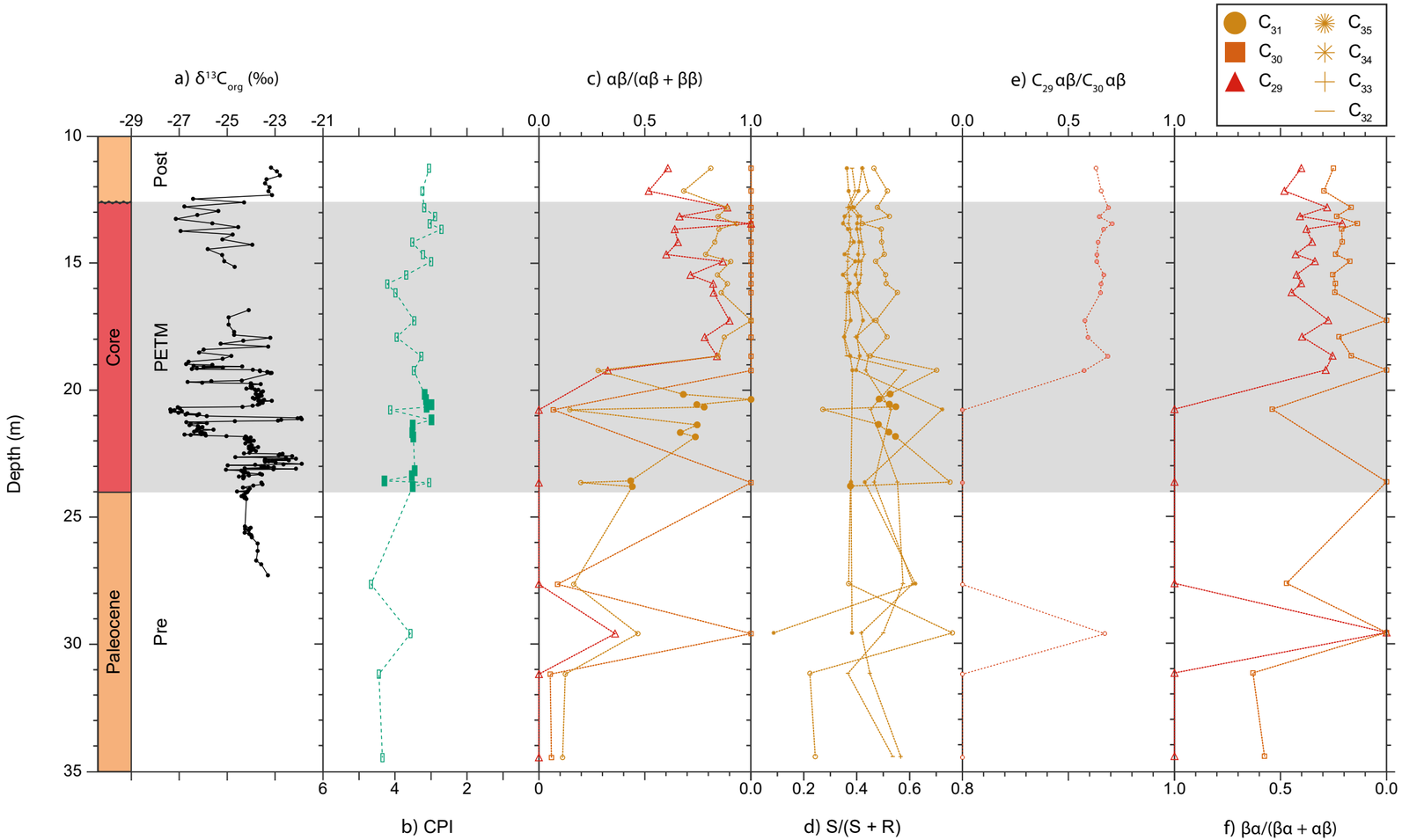
a) δ13Corg (‰)
c) αβ/(αβ + ββ)
e) C29 αβ/C30 αβ
C31
C30
C29
C35
C34
C33
C32
Depth (m)
Core
Paleocene
Post
PETM
Pre
b) CPI
d) S/(S + R)
f) βα/(βα + αβ)

**Figure 7.**

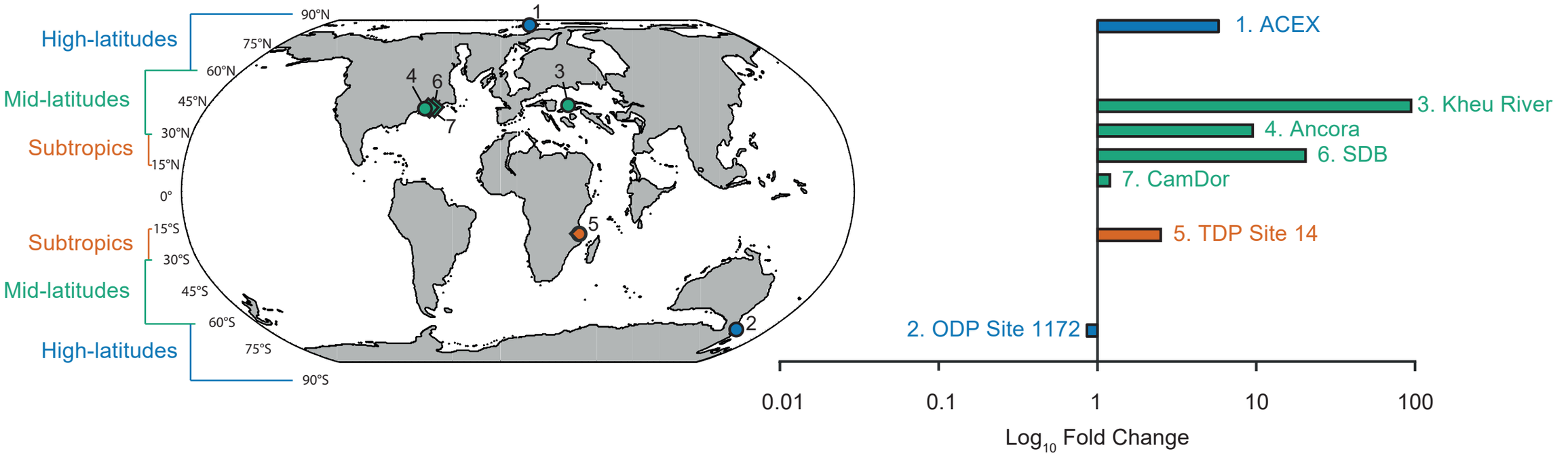
High-latitudes
Mid-latitudes
Subtropics
Subtropics
Mid-latitudes
High-latitudes
90°N
75°N
60°N
45°N
30°N
15°N
0°
15°S
30°S
45°S
60°S
75°S
90°S
1
2
3
4
5
6
7
1. ACEX
2. ODP Site 1172
3. Kheu River
4. Ancora
5. TDP Site 14
6. SDB
7. CamDor
0.01
0.1
1
10
100
Log10 Fold Change

**Figure 8.**

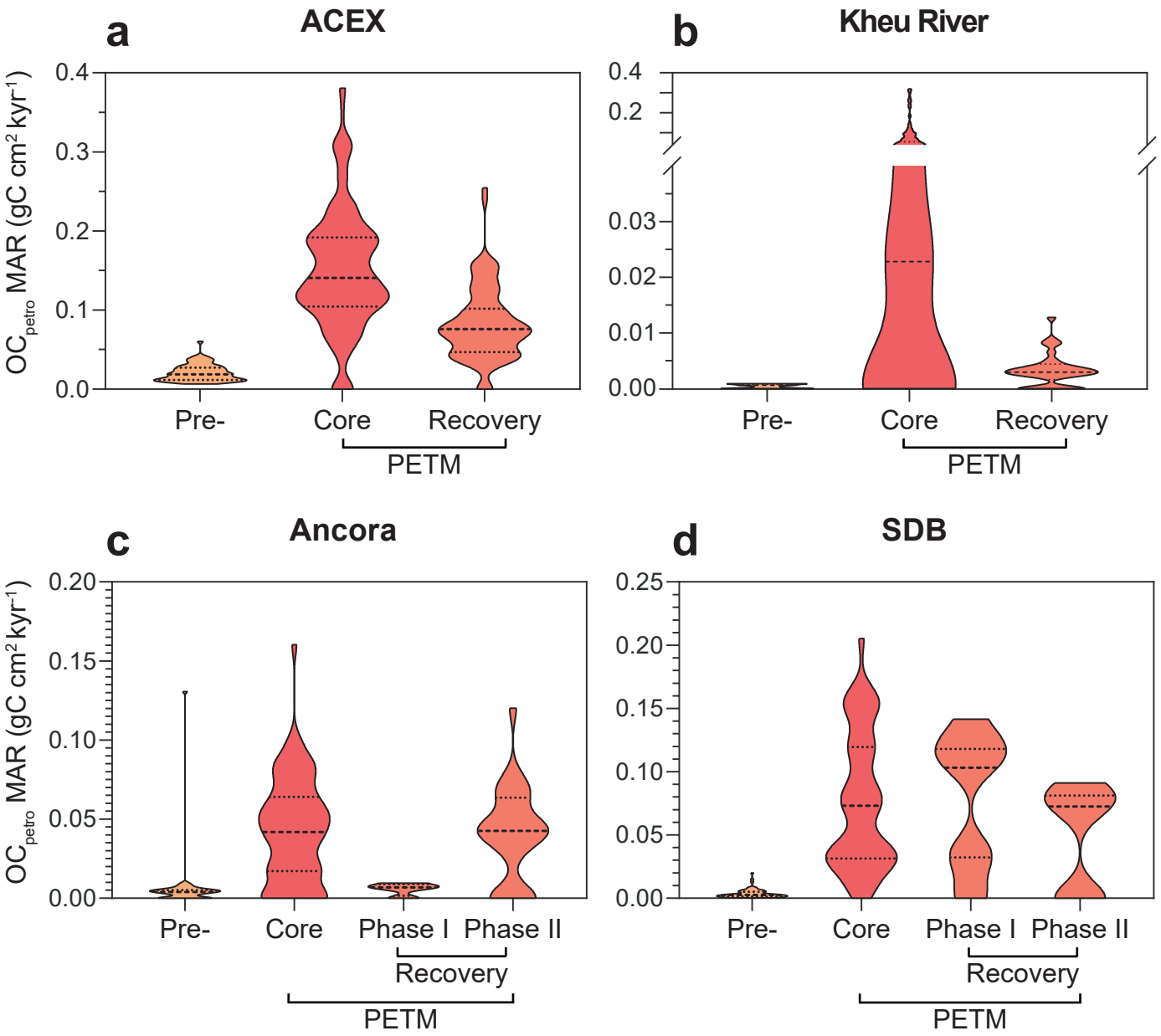
a
ACEX
b
Kheu River
c
Ancora
d
SDB
OC petro MAR (gC cm2 kyr-1)
Pre-
Core
Recovery
Phase I
Phase II
PETM